Biointerface Research in Applied Chemistry
Open-Access Journal (ISSN: 2069-5837)

Article
Volume 13, Issue 3, 2023, 235
https://doi.org/10.33263/BRIAC133.235

Computational Investigation on the Efficiency of Small Molecule Inhibitors Identified from Indian Spices against SARS-CoV-2 Mpro

Chainee Das [1], Dorothy Das [1], Venkata Satish Kumar Mattaparthi [1,*]

[1] Molecular Modeling and Simulation Laboratory, Department of Molecular Biology and Biotechnology, Tezpur University, Tezpur, Assam, 784028, India; chaineedas97@gmail.com (C.D.); dorthyds.1010@gmail.com (D.D.); mvenkatasatishkumar@gmail.com, venkata@tezu.ernet.in (V.S.K.M.);
* Correspondence:mvenkatasatishkumar@gmail.com, venkata@tezu.ernet.in(V.S.K.M.);

Scopus Author ID 54962670000
Received: 1.01.2022; Accepted: 5.02.2022; Published: 6.06.2022

Abstract: Recently, small compounds from Indian spices (Carnosol, Arjunglucoside-I, and Rosmanol) have been identified as SARS-CoV-2 main protease (Mpro) inhibitors. The structural dynamics and characteristic features of binding of these small molecules to the SARS-CoV-2 Mpro are not well understood. Here, we have constructed the potential of mean force (PMF) for dissociating Mpro-small molecule inhibitor complexes from the umbrella sampling simulations using the weighted histogram analysis method. Mpro-small molecule inhibitor complexes exhibited relatively higher dissociation energy values than the alpha-ketoamide-Mpro complex (positive control) from the PMF calculations. We found that binding affinity between protein and ligand is higher in Mpro-Arjunglucoside-I complex [ΔG_{bind} = -19.74 kcal mol^{-1} from MM-GBSA and ΔG_{bind} = -9.13 kcal mol^{-1} from MM-PBSA] than in other three SARS-CoV-2 small molecule complexes. The MM-GBSA/MM-PBSA calculations revealed that the small molecule inhibitors studied in this work have substantially higher binding affinity for Mpro. We found the residues present in SARS-CoV-2 Mpro's binding pocket contributed the most binding free energy to SARS-CoV-2 Mpro-small molecule interactions. Our findings emphasize the structural and binding features of the identified small molecule inhibitors with SARS-CoV-2 Mpro, which could be relevant in developing therapeutic candidates to combat SARS-CoV-2.

Keywords: MM-GBSA; MM-PBSA; **the** potential of mean force; molecular dynamics; per residue energy decomposition; COVID 19.

1. Introduction

A unique strain of SARS-CoV-2 coronavirus was first detected in Wuhan, a city in China's Hubei Province with a population of 11 million people, in December 2019, following a pneumonia outbreak with no clear reason. The virus has spread to more than 200 countries and territories around the world, and on March 11, 2020, the World Health Organization (WHO) declared it a pandemic[1, 2]. There was 288,767,991 laboratory-confirmed coronavirus disease 2019 (COVID-19) infection worldwide as of the 1st of January 2022, with 5,455,634 recorded fatalities. On 16 March 2020, outside of China, the number of cases and deaths surpassed those within the country [3]. SARS-CoV-2 belongs to the coronavirinae family of single-stranded RNA viruses, divided

into four genera: alpha, beta, gamma, and delta [4, 5]. The majority of this family's members are enzootic, with only a few species infecting humans (namely alpha and beta coronaviruses). It also causes minor infections in people, akin to the common cold, and is responsible for 10-30% of upper respiratory tract infections in adults. More severe infections are uncommon, but enteric and neurological diseases may be caused by coronaviruses [6]. A coronavirus might generally take up to two weeks to incubate [7]. Middle East Respiratory Syndrome (MERS), first reported in September 2012 in Saudi Arabia, and Severe Acute Respiratory Syndrome (SARS), first reported in 2003 in southern China, are two previous coronavirus outbreaks. MERS infected almost 2,500 people, resulting in more than 850 deaths, while SARS infected over 8,000 people, resulting in approximately 800 deaths. The case fatality rates were 35 percent and 10 percent for these conditions, respectively. SARS-CoV-2 is a novel coronavirus strain that has never been found in humans before. Although the incubation period of this strain is currently unknown, the US Centers for Disease Control and Prevention advise that symptoms can appear as soon as 2 days after exposure and as late as 14 days after exposure [7].

The current pandemic predicament has prompted the scientific community to conduct a time-sensitive quest for effective antiviral therapy techniques. Computational techniques are one of the most extensively used approaches for detecting potential therapeutic agents. Several drug-like or lead-like candidates have been found or repurposed against the SARS-CoV-2 drug target proteins.

It is well known that viruses that cause human disease encode one or more proteases, which are essential components of the viral life cycle. Proteases are the ideal therapeutic targets for viral infections because they cleave the viral polyprotein, allowing the virus to continue to replicate [8, 9]. In cases where the virus has evolved mutational resistance, protease inhibitors have been employed along with the drug treatment. Protease inhibitors were utilized in conjunction with nucleoside reverse transcriptase to treat viral disorders such as acquired immunodeficiency syndrome, and this combination therapy method to overcome drug resistance was successful. The SARS-CoV-2 replicase enzyme encodes pp1a and pp1ab polyproteins, which create all functional polypeptide units required for replication and transcription. The catalytic cleavage action of 3CLpro releases polypeptides at different subsites of polyproteins. For all coronaviruses, this cleavage mechanism is retained in 3CLpro. The protease 3CLpro has been identified as a possible therapeutic target for COVID-19 therapy due to its important role in viral replication and the lack of a similar homolog in humans [10-22]. SARS-CoV-2 Mpro plays a critical function in the processing of polyproteins transcribed from viral RNA, and therefore this protease is viewed as a key to critical survival and development. Despite its potential, the search for 3CLpro inhibitors that could be used to treat COVID-19 has so far been unsuccessful. For the COVID-19 treatment, many computational studies have focused on currently available antiviral medicines [23-42] targeting the viral replication process.

Computer-aided drug discovery technologies have developed as crucial and powerful tools in the drug development process over the last decade. They have been used to uncover protein inhibitors and analyze protein-drug and protein-protein interactions. Because turning a candidate drug into an approved drug is a time-consuming and costly process. A combination of computer methodologies such as virtual screening, docking, molecular dynamics (MD) simulation, and binding free energy evaluation can help identify potential drug candidates from compound

libraries. Many *in silico* studies have been conducted to identify potential SARS-CoV-2 inhibitors. In one of the studies, using the virtual screening method, small chemical molecules (Carnosol (CAN), Arjunglucoside-I (ARJ), and Rosmanol (ROS)) from Indian spices have been identified, and the results showed that they have the capacity to inhibit SARS-CoV-2 Mpro and may have antiviral properties against nCoV [43]. Furthermore, anti-carcinogenic activities have been reported for these small chemical compounds [44-46]. However, more research into these inhibitors' effects on SARS-CoV-2 Mpro is needed before clinical trials may be undertaken.

In this study, we used the potential of the mean force method to show these small molecule inhibitors' likely binding (unbinding) approach with SARS-CoV-2 Mpro during the formation (dissociation) of the corresponding complex in terms of free energy as a function of the reaction coordinate.

We employed molecular docking and molecular dynamics simulations to study the binding interaction of the small molecule inhibitors with SARS-CoV-2 Mpro. These small molecule inhibitors SARS-CoV-2 Mpro complexes were subjected to binding free energy calculations and a per-residue energy breakdown study. The molecular mechanics Poisson Boltzmann surface area (MM-PBSA) and the molecular mechanics Generalized Borne Surface area (MM-GBSA) approaches were applied to compute the binding free energy and identify the residues of Mpro involved in interaction with the small molecule inhibitors. The MM-GBSA/MM-PBSA calculations exhibited that the small molecule inhibitors considered in this study showed a marked binding affinity with Mpro compared to the positive control (P3-Capped alpha-ketoamide inhibitor 40 (AKA)). In this study, we have considered AKA a positive control because recently, AKA was reported to be more potent than anti-HIV retroviral drugs such as lopinavir and darunavir [21]. The contribution of each residue to the binding free energy was examined to gain a better knowledge of the binding features of Mpro-small molecule inhibitor complexes. Our findings emphasize the structural and binding features of the identified small molecule inhibitors with SARS-CoV-2 Mpro, which could be relevant in developing therapeutic candidates to combat SARS-CoV-2.

2. Materials and methods

The methods and their objectives carried out in this work have been briefed in a flow diagram Supplementary (Figure S1).

2.1. Initial structure preparation and molecular docking.

2.1.1. Preparation of receptor (SARS-CoV-2 Mpro).

The receptor molecule for docking purposes was the 3-D structure of the SARS-CoV-2 Mpro with an unliganded active site (PDB ID: 6y84 with a resolution of 1.39 Å) which was obtained from the Research Collaboratory for Structural Bioinformatics Protein Data bank (www.rcsb.org) [47].

2.1.2. Preparation of ligands.

The Chemical structures of the ligands, namely (i) Alpha-ketoamide (positive control) (ii) Arjunglucoside-I (iii) Carnosol, and (iv) Rosmanol in SDF format, were retrieved from PubChem online server details are summarized in Table 1. The Open bable server was used to convert the SDF format of these small molecules to PDB format.

2.2. Preparation of the SARS-CoV-2 Mpro-ligand complexes.

The receptor molecule (SARS-CoV-2 Mpro) retrieved from Protein Data Bank was then docked to the ligands (Alpha-ketoamide, Arjunglucoside-I, Carnosol, and Rosmanol) using the PatchDock/Firedock [48] online docking server. PatchDock employs a structure-based molecular docking technique. The PatchDock algorithm splits the protein molecules' Connolly dot surface representation into three classes: convex, concave, and flat patches [49, 50]. The candidate transformations were then created by combining complementary patches.

Table 1. Details of the small molecule inhibitors obtained from the PubChem database.

S.no.	Name of small molecule	PubChem-ID	Structure
1.	Alpha-ketoamide (AKA)	6481510	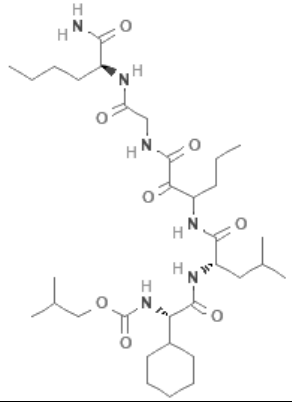
2.	Arjunglucoside-I (ARJ)	14658050	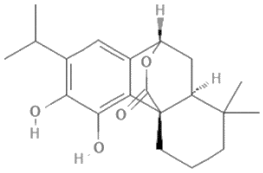
3.	Carnosol (CAN)	442009	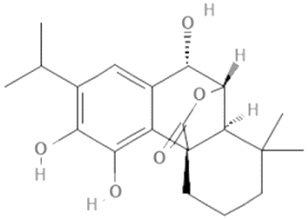
4.	Rosmanol (ROS)	13966122	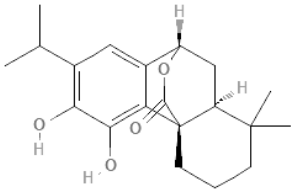

A scoring function that includes the atomic desolvation energy and the geometric fit is also applied to evaluate each candidate transformation. First, the candidate solutions use root-mean-

square deviation (RMSD) clustering to eliminate the redundant solution. The PDB coordinate files of protein and ligand molecules are used as input parameters for docking. In the PatchDock analysis, three key processes are followed: (i) surface patch matching, (ii) molecular shape representation, and (iii) filtering and scoring. From the PatchDock server, many resulting docked model complexes were generated for the four SARS-CoV-2 Mpro-ligand complex systems. The initial complex structure was chosen based on its atomic contact energy (ACE), geometric surface, and geometric shape complementarity score in all four complex systems. Using UCSF Chimera [51], the complex structure was examined, the ligand and receptor sections were separated, and their coordinates were stored in mol2 and PDB formats, respectively. Using the antechamber protocol, the selected solution structure was further curated in xleap. This includes bcc charge addition, frcmod file generation, and PDB formats.

Using the antechamber protocol, the selected solution structure was further curated in xleap. This includes bcc charge addition, frcmod file generation, and complex system in explicit and implicit solvation. The topology and coordinate files for each of the four complex systems were then prepared individually.

2.3. MD simulation of receptor-ligand complexes.

The initial coordinate and topology file for the separated receptor and ligands structures for all four complexes were produced using the AMBER ff99SB force field and the Leap module of the AMBER 14 software package. The receptor and its ligand were then loaded together. The coordinate and topology files of the loaded receptor-ligand complex were created using the Leap module in both implicit and explicit environments. The loaded system was solvated in all directions with the TIP3P [52] water model with a solvent buffer of 10 Å. The complex's charge was then neutralized by adding the appropriate number of counterions.

The four receptor-ligand complexes were then subjected to energy minimization in two phases using the AMBER 14 software package. The first 500 steps of steepest descents minimization (while preserving restraints over the solute) and the second 500 steps of conjugate gradient minimization (devoid of restraints on the solute).

The MD experiment was carried out according to a standard technique, which included heating dynamics, density, equilibration, and production dynamics. We used energy minimized receptor-ligand system as the starting structure for ensuing MD steps. The density procedure was performed after the individual receptor-ligand system was gradually heated from 0-300 K in constant volume (NVT) conditions. Later the system was equilibrated for 1 ns in NPT conditions (300 K and 1 atm pressure). The density, temperature, pressure, and energy graphs were plotted and examined to guarantee the system's successful equilibration. Then, applying the Particle Mesh Ewald (PME) method [53, 54], we ran a 10 ns MD production run for the equilibrated structure of the receptor-ligand system with a time step of 2 fs. During the simulation, a cut-off of 8 Å was used to tackle nonbonding interactions (short-range electrostatic and van der Waals interactions), whereas the PME approach was used to treat long-range electrostatic interactions. The SHAKE algorithm [55] was used to constrain all of the bonds in the system. The Berendsen weak coupling algorithm [56] maintained the pressure and temperature (0.5 ps of heat bath and 0.2 ps of pressure relaxation) constant throughout the simulation.

After the 10 ns of production dynamics of the four receptor-ligand complexes were completed, the RMSD clustering algorithm was used to extract the lowest energy conformer of each individual complex from the densely populated clusters, followed by the measurement of the center of mass(es) (CoM) distance between the receptor and the ligand in the complex structure. The extracted structures of each of the four complexes were then used as the starting point for PMF [57] analysis.

2.4. PMF calculation.

AMBER software was used to create PMF [38] for the four small-molecule inhibitor complexes of SARS-CoV-2 Mpro utilizing Alan Grossfield's Weighted Histogram Analysis Method (WHAM) [58] employing umbrella sampling (US) [59] simulations. PMF is used to determine free energy along a certain reaction coordinate, and this free energy profile aids in the identification of transition states, intermediates, and relative endpoint stabilities. However, simply running the MD simulation to generate free energy along the reaction coordinate will not generate accurate PMF because the energy barrier of interest is many times the size of kbT, so the MD simulation will either stay in the local minimum it started in or cross to different minima, rarely sampling the transition state. US sampling strategy is used with WHAM [48], which helps attain the interest samples' transition states. The reaction coordinates for the four small-molecule inhibitor complexes of SARS-CoV-2 Mpro were divided into a series of windows by the US, and then restraints were given to the samples to keep them close to the center of the window, ensuring that the samples were kept close to that the endpoints overlapped. The Hamiltonian was then augmented with biassing potentials to limit the molecular system to certain regions of phase space. The biassing potential is typically a harmonic potential that keeps the system close to a specified value in the reaction path. This was carried out in several windows throughout the reaction path. Equilibrium simulations were run in each window, and the biased probability distribution (histogram) was calculated. The optimal free energy constants for the combined simulations are then determined using the WHAM.

The PMF calculation for studying the degree of association between the corresponding small molecule inhibitor and the SARS-CoV-2 Mpro was done by increasing and decreasing the CoMs distance between the corresponding small molecule inhibitor and the SARS-CoV-2 Mpro in two separate directions from the starting point. The CoMs distance between the small molecule inhibitor and the SARS-CoV-2 Mpro was altered from 8 Å to 25 Å in all four small-molecule inhibitor complexes of SARS-CoV-2 Mpro, spanning diverse configurations. Because the buffer of water is 10 Å out of solute, it is expected that a component of the complex structure will emerge out of the solvation box for bigger distances of separation (more than 15 Å) of the ligand and receptor units in the complex. So, at a wider umbrella sampling distance (for each window of the US simulation), we took the solute (complex) and resolved it with TIP3P water molecules with a solvent buffer of 10 Å enclosing the complex from all sides, as well as neutralized the system with counterions. Before the US simulation, we ensured that the complex system's periodic boundary conditions and equilibration were in place. The system was run for 5 ns of MD simulation with harmonic potentials at each distance of the US window to keep the CoM distance between the two monomeric units near the required values. For all four small-molecule inhibitor complexes of SARS-CoV-2 Mpro, we calculated the PMF as a function of the reaction coordinate.

2.5. MD simulation of the structure with the lowest energy of the SARS-CoV-2 Mpro- small molecule inhibitor complexes.

A structure with the lowest potential energy was chosen from the ensemble of related SARS-CoV-2 Mpro small molecule inhibitor complex structures at the reaction coordinate corresponding to the minimum PMF values and then subjected to MD simulation to examine its prominent structural features. Then the same conventional approach was utilized for minimization, heating, density, equilibration, and production dynamics of the lowest energy structure of the SARS-CoV-2 Mpro- small molecule inhibitor complexes, but with a 50 ns modification in the duration of the production run. The PTRAJ (short for Process TRAJectory) and CPPTRAJ (a rewriting of PTRAJ in C++) modules [60] of AMBER 14 Tools were used to evaluate the MD trajectories for the four complexes. To assess the convergence of the four complex systems, we looked at the RMSDs for the ligand and complex, using the corresponding initial structure as a reference. We also calculated the RMSFs and Rg to examine the four complexes' flexibility and size. In addition, intermolecular hydrogen bond analyses were carried out for each of the four complexes to see how the complex's stability is altered during MD simulation.

2.6. Binding free energy (BFE) analyses for the four SARS-CoV-2 Mpro- small molecule inhibitor complexes.

The four SARS-CoV-2 Mpro-small molecule inhibitor complexes were subjected to BFE investigations. The MMPBSA.py script [61] of the AMBER 14 suite was used to calculate the relative BFE and per-residue energy decomposition (PRED) of the interface residues of the four complexes in this work. The Molecular Mechanics-Poisson-Boltzmann Surface Area (MM-PBSA) and Molecular Mechanics-Generalized Borne Surface Area (MM-GBSA) algorithms are used to create this script. To determine the binding free energy (ΔG_{bind}) and comprehend the roles of electrostatic and van der Waals terms in the formation of complexes, the MM-PBSA/GBSA methods were used.

The equations (1-6) show the formulas for computing the BFE and their decomposed energy components. The free energy difference between the bound state complex ($G_{complex}$) and the free state individuals of the receptor ($G_{receptor}$) and ligand (G_{ligand}) is represented by the total BFE (ΔG_{bind}). ΔG_{bind} can be divided into enthalpy (ΔH) and entropy ($-T\Delta S$) using the second law of thermodynamics. The enthalpies were determined with a low computing effort using Poisson–Boltzmann or Generalized-Born surface area continuum solvation (MM-PBSA/MM-GBSA) method [62, 63], and the entropy was evaluated using normal mode (nmode) analysis [64, 65]. After calculating MM-PBSA/MM-GBSA using all of the trajectories, three components of the individual four complexes were analyzed: (i) ligand (ii) receptor (iii) complex. Many recent in-silico investigations [66-76] have employed the methodologies and protocols that we evaluated in this study to estimate the binding free energy.

BFE for the four complex systems was calculated using Eqn. (1):

$$\Delta G_{binding} = \Delta G_{complex} - [\Delta G_{receptor} + \Delta G_{ligand}] \quad (1)$$

where $\Delta G_{binding}$ is the total binding free energy.

Thermodynamically:

$$\Delta G = \Delta H - T\Delta S \quad (2)$$

$$\Delta G = \Delta E_{MM} + \Delta G_{sol} - T\Delta S \quad (3)$$

$$\Delta E_{MM} = \Delta E_{int} + \Delta E_{ele} + \Delta E_{vdw} \quad (4)$$

and

$$\Delta G_{sol} = \Delta E_{PB/GB} + \Delta E_{SURF} \quad (5)$$

$$\Delta E_{SURF} = E_{NP} + E_{dis} \quad (6)$$

2.7. Enthalpy calculations with MM-GBSA/PBSA.

$\Delta G_{complex}$, $\Delta G_{receptor}$ and ΔG_{ligand} indicate free energy contributions from small molecule inhibitor-SARS-CoV-2 Mpro (complex), SARS-CoV-2 Mpro (receptor), and small-molecule inhibitor (ligand) for the four complex systems, as given in Eqn. (1).

As stated in Eqn. (3) the enthalpy portion is derived by adding the change in molecular dynamics energy (ΔE_{MM}) and the solvation free energy (ΔG_{sol}). ΔE_{MM} is composed of internal energy (Δ_{Eint}) (bond, angle, and dihedral energies), electrostatic interaction (ΔE_{ele}), and van der Waals interaction (ΔE_{vdw}). The solvation-free energy is divided into polar ($\Delta E_{PB/GB}$) and non-polar (ΔE_{SURF}) contribution Eqn. (5). $\Delta E_{PB/GB}$ is derived using Poisson-Boltzmann/Generalized-Boltzmann models, and ΔE_{SURF} is the sum of non-polar contribution calculated by PB (E_{NP}) and dispersion energy (E_{dis}) using Solvent accessibility surface area (SASA).

2.8. Conformational entropy calculation based on nmode.

The normal mode analysis [64, 65] and the python-based mmpbsa py nabnmode tool were used to compute the conformational entropy ($T\Delta S$) during the interaction of receptor and ligand units in the four complexes. The normal modes for the complex, receptor, and ligand were determined and then averaged to obtain a binding entropy estimate in this study. The PRED analysis calculates the energy contribution of each protein residue by examining its molecular interactions across all of the complex's residues.

3. Results and Discussion

3.1. PMF profile of SARS-CoV-2 Mpro-ligand complexes.

To analyse the unbinding pathway of each of these small molecule inhibitors and the positive control AKA from the SARS-CoV-2 Mpro, a PMF study was done by combining MD simulations with the umbrella sampling (US) method [77, 59]. The equilibrated complex structure of Mpro –AKA/other small molecule inhibitors (ARJ, CAN, ROS) were chosen as the starting structure for the US simulation. We plotted the density, temperature, potential energy, kinetic energy, and total energy of the AKA/small molecules-SARS-CoV-2 Mpro complex as a function of simulation time to ensure that our NPT simulation algorithm was correct shown in Supplementary (Figures S2, S3, S4, and S5).

Figure 1 shows the PMF profile for Mpro – AKA/ small molecules (ARJ, CAN, ROS) in water at normal temperature as a function of the reaction coordinate. The reaction coordinate is

defined as the distance between the AKA/small molecules and SARS-CoV-2 Mpro centers of mass. For the Mpro – AKA/ small molecules, 5 ns simulations were performed for each window to assure the sampling convergence of US simulations. And as shown in Supplementary (Figure S6), after each nanosecond of simulations, the convergence of PMF was assessed. The strategy that we have employed to check the convergence of PMF was the standard one and used in earlier works [78].

The PMF depths from the US simulation of SARS-CoV-2 Mpro small-molecule systems were found to be larger than those from the SARS-CoV-2 Mpro-AKA complex system (Figure 1), indicating a deeper energy potential depth and hence a longer residence period of the small molecules in the SARS-CoV-2 Mpro binding pocket.

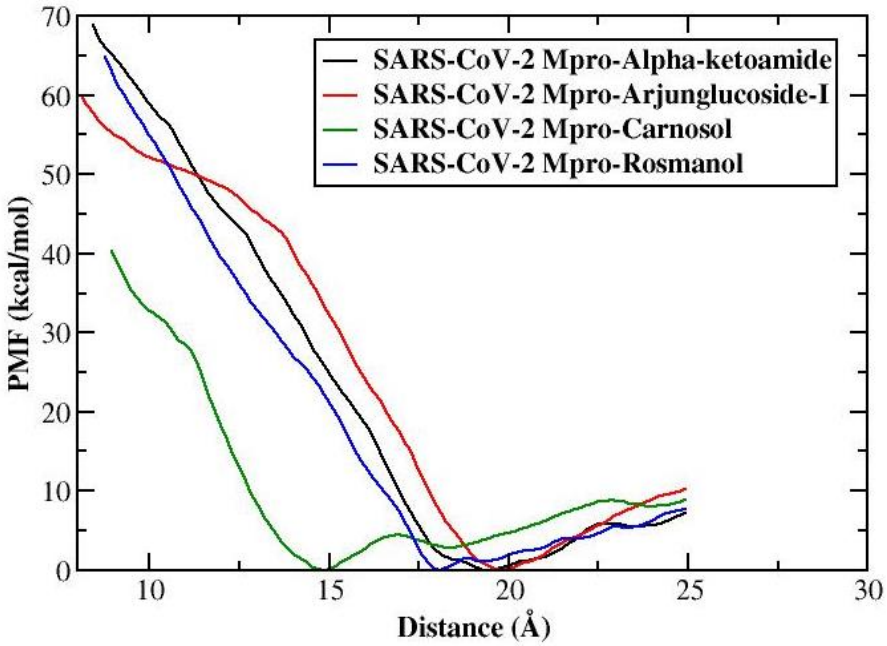

Figure 1. Potential of mean force for the association and dissociation of the SARS-CoV-2 Mpro-small molecule complexes.

We observed the use of distinct reaction coordinates (RCs) when small molecules dissociate from the AKA binding pocket of SARS-CoV-2 Mpro, as stated according to a comparative study of PMF curves. When ligands (small molecule inhibitors) moved out of the AKA binding pocket of SARS-CoV-2 Mpro, different phases of vertical elevation of the PMF (Figure 1) were observed. The small molecules were seen to move out of the AKA binding pocket when the biased potential rises. In the case of the Arjunglucoside-I small molecule inhibitor (Figure 1), when the ligand moves out of the binding pocket of SARS-CoV-2 Mpro, the PMF of RCs is upgraded. At 20 Å of RC, the ligand completely dissociates with a potential energy value of 12 kcal/mol. Similarly, as the PMF curve rises, the other small molecule inhibitors are seen gradually moving out of the binding pocket of SARS-CoV-2 Mpro (Figure 1). We detected an energy barrier when the AKA small molecule was unbound from the binding pocket of SARS-CoV-2 Mpro and at 22.0 Å of RC, with a potential energy value of 8 kcal/mol, AKA dissociates from its binding site far more easily than other small molecule inhibitors. The snapshots of all the complex systems taken at various windows of separation distances during the simulation were shown in Supplementary (Figures S7, S8, S9, and S10).

The PMF profiles of all small molecule inhibitors and AKA with SARS-CoV-2 Mpro were compared. According to PMF plots, AKA has the lowest dissociation energy barrier of all the small molecules investigated here and is thus expected to be easily released from the binding site of SARS-CoV-2 Mpro. The order of dissociation of small-molecule inhibitors from the AKA binding site of SARS-CoV-2 Mpro was determined by PMF plots to be AKA < Rosmanol < Carnosol < Arjunglucoside-I.

From Figure 1, we see that the four small-molecule- SARS-CoV-2 Mpro complexes show the minimum PMF values at different separation distances and exhibit different dissociation energy values in kcal mol^{-1}. The results have been summarized in Table 2.

Table 2. Details of Umbrella Sampling Simulation.

S.no.	Name of the complex	Equilibrium distanc (Å) at minimum PMI value	Dissociation energy (kcal/mol)	Distance samples (Å)	Duration (ns)for umbrell sampling, each window sid being 5ns.
1.	AKA- SARS- CoV2 MAIN PROTEASE	19.5	9	8-25 Å	90 ns
2.	ARJ- SARS- CoV2 MAIN PROTEASE	20	11	8-25 Å	90 ns
3.	CAN- SARS- CoV2 MAIN PROTEASE	15	10	8-25 Å	90 ns
4.	ROS- SARS- CoV2 MAIN PROTEASE	17.5	9.5	8-25 Å	90 ns

When the distance between the small molecule inhibitors and the SARS-CoV-2 Mpro crosses 22 Å, we noticed no more interactions between them. The PMF was observed to increase when the inter-molecular distance between SARS-CoV-2 Mpro and the small molecules was lowered below the optimum equilibrium distance (15 Å in the case of Carnosol, 18 Å in the case of Rosmanol, 19 Å in the case of Arjunglucoside-I and Alpha-ketoamide).

3.2. Salient structural features of the minimum PMF structure of the small molecule inhibitors-SARS-CoV-2 Mpro complex.

3.2.1. Molecular dynamics analysis.

Because it works with atomic-level interactions, MD is a useful computational tool for deciphering the physical foundation of biological macromolecule structure and function. From their corresponding 50 ns MD simulation trajectories, changes in the structure and stability of small molecule inhibitors-SARS-CoV-2 Mpro complexes were investigated. The trajectories obtained from 50 ns simulation for SARS-CoV-2 Mpro complexed with AKA (positive control), Arjunglucoside-I, Carnosol, and Rosmanol were analyzed using the CPPTRAJ module of the Amber program. The 3-D structure of the four complexes isolated at their minimum PMF value was used as starting structure for the corresponding simulation.

3.3. Stability profile analysis of the SARs-CoV-2 Mpro protein-ligand complexes.

The dynamic stability and structural behavior of the SARS-CoV-2 Mpro-small molecule inhibitor complexes were investigated using MD simulations. The MD simulation data trajectory files were obtained over a 50-ns simulation time period.

3.3.1. RMSD analysis.

The atom-positional root-mean-square deviation (RMSD) generated by roto-translational least-squares fitting is perhaps the most widely used for structural comparison and stability measure. The degree of structural variability in a particular ensemble is captured by RMSD values, which can be related to the intrinsic flexibility of a specific structure or the uncertainty of the structural refinements. The arithmetic mean is frequently used to summarise the parameters of this distribution, which is typically determined for backbone atoms. RMSD from the starting structure for the C-α backbone atoms from all the residues of Mpro complexed with AKA (positive control), Arjunglucoside-I, Carnosol, and Rosmanol were calculated (Figure 2) from the 50 ns MD simulations. The simulation findings showed that when the Mpro was complexed with the small molecule inhibitors, the final RMSD variation from the initial model of C- and backbone atoms showed stable conformation, which was maintained throughout the simulation time of 50 ns. RMSD plots of Mpro complexed with the four ligands were similar, ranging between 0.7 Å and 1.7 Å. The fluctuation amplitude and the modest change in the average RMSD value of the C-backbone atoms clearly show that the four SARS-CoV-2 Mpro protein-ligand complex structures have a stable dynamic behavior. In the four complexes, we have also calculated the RMSD of the four small molecule inhibitors (Figure 3) to check whether they are stable in the active site of SARS-CoV-2 and identify their possible binding modes. From the RMSD analysis of ligands, we found that AKA showed larger fluctuations in the RMSD values among the four ligands. So the small molecule inhibitors identified from Indian spices are stable in the active site compared to the positive control.

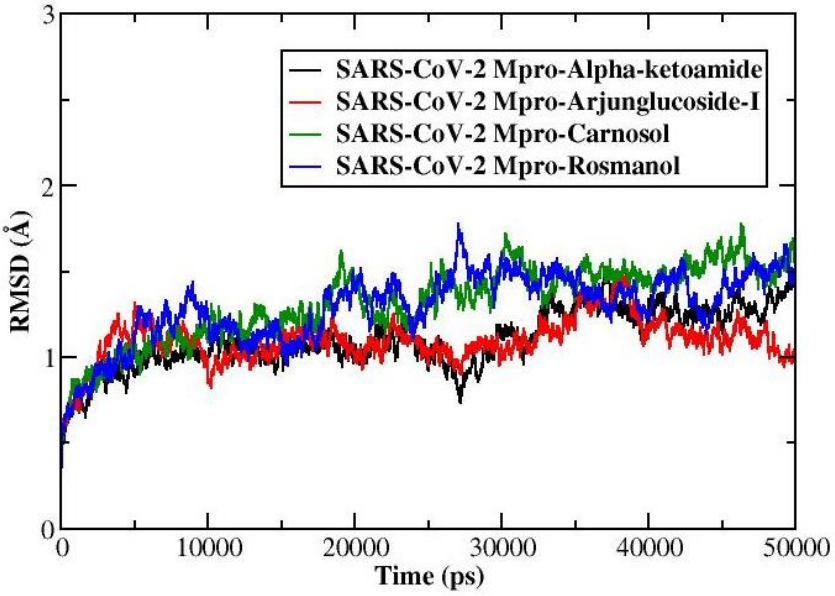

Figure 2. Root Mean Square Deviation (RMSD) analysis of the SARS-CoV-2 Mpro-small molecule inhibitor complexes as a function of simulation time in picoseconds.

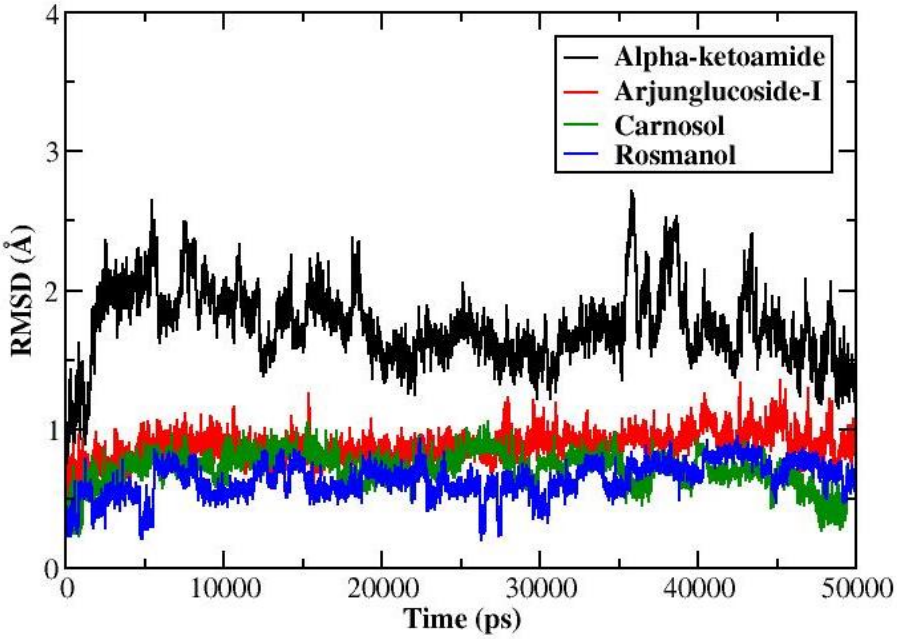

Figure 3. Root Mean Square Deviation (RMSD) analysis of the small molecule inhibitors in the complexes as a function of simulation time in picoseconds.

3.3.2. RMS Fluctuation (RMSF) of Protein.

Residues root mean square fluctuation (RMSFs) analysis was used to determine the residues responsible for complex structural fluctuations in the four SARS-CoV-2 Mpro complexes (Figure 4). The average position of fluctuations of all the Cα-atoms in the amino acid residues of the complex is depicted by RMSF analysis. In all the four SARS-CoV-2 Mpro-ligand complexes, greater fluctuations were observed at the residues near the binding site of the ligand.

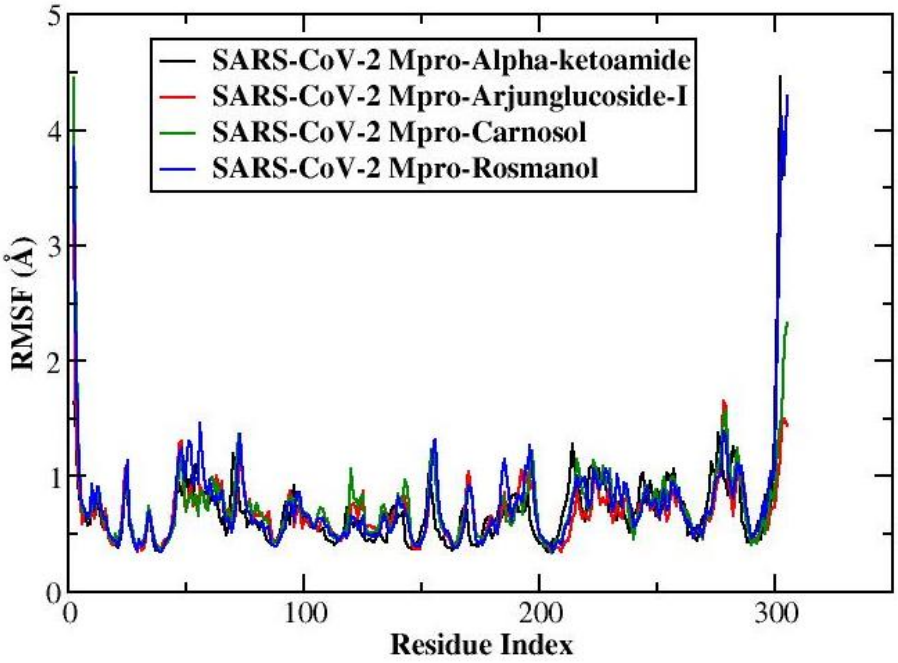

Figure 4. Root Mean Square Fluctuation (RMSF) Analysis of the SARS-CoV-2 Mpro-small molecule inhibitor complexes as a function of Residue index.

3.3.3. Radius of gyration analysis.

The mass-weighted root-mean-square distance of atoms from their center of mass is known as the radius of gyration (Rg). (Figure 5) depicts the information about the compactness, shape, and folding of the four complex structures at various point scales throughout the 50 ns of MD simulation trajectory. Throughout the 50 ns simulation time, all four complexes showed a similar pattern in terms of Rg value. It denotes the four complexes' long-term stability and compactness.

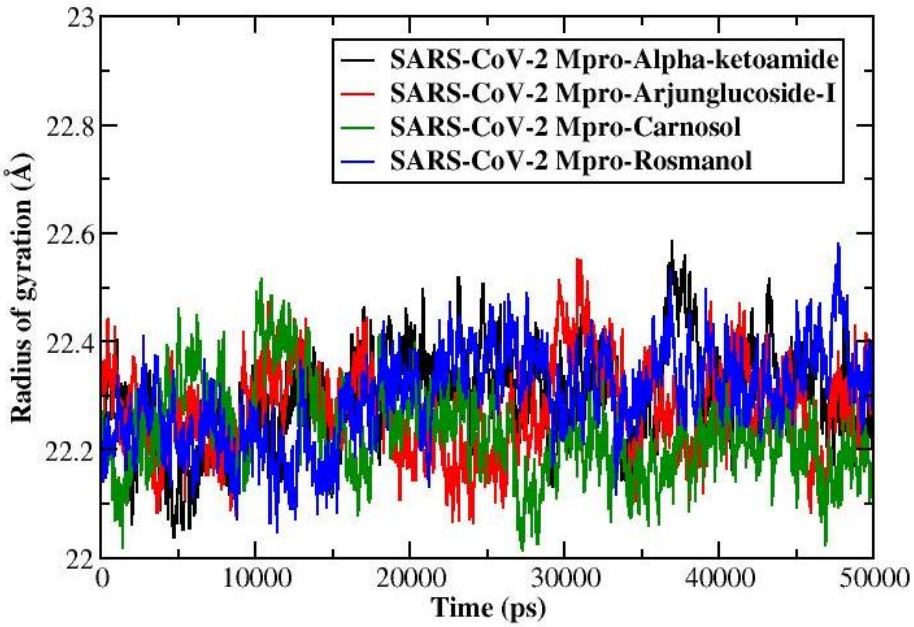

Figure 5. The radius of gyration analysis (Rg) of the SARS-CoV-2 Mpro-small molecule inhibitor complexes as a function of simulation time in picoseconds.

3.4. Protein-ligand contact profiles.

The protein-ligand interaction patterns for all ligands with SARS-CoV-2 Mpro were obtained from the MD simulation trajectories, as shown in Supplementary (Table S1-S4 and Figure S11). During the 50 ns simulation of the SARS-CoV-2 Mpro alpha-ketoamide complex, we found the residues GLU165, LEU166, PRO167, GLN188, ASN141, SER143, HIE162, HIE163, MET48, THR26 of SARS-CoV-2 Mpro have been involved in interaction with the ligand via hydrogen bonding, hydrophobic, ionic, and water bridge interactions. In other small molecule inhibitors-SARS-CoV-2 Mpro complexes, during the 50 ns of simulation, residues around the active site of Mpro were involved in interactions with the ligands via hydrogen bonding, hydrophobic, ionic, and salt bridge interactions. In addition, we have also determined the total number of intermolecular hydrogen bonds at different points throughout the 50 ns simulation time in the four complexes, as shown in (Figure 6). Individual occupancies of detected H-bonds per ligand are detailed in Supplementary Tables (Table S5-S8). From the plots, we can see for the four complexes, the number of intermolecular hydrogen bonds follows the order SARS-CoV-2 Mpro-Arjunglucoside > SARS-CoV-2 Mpro-Carnosol > SARS-CoV-2 Mpro-Alpha-ketoamide > SARS-CoV-2 Mpro-Rosmanol. These observations suggested the ligands from Indian spices as a strong inhibitor against SARS-CoV-2 Mpro.

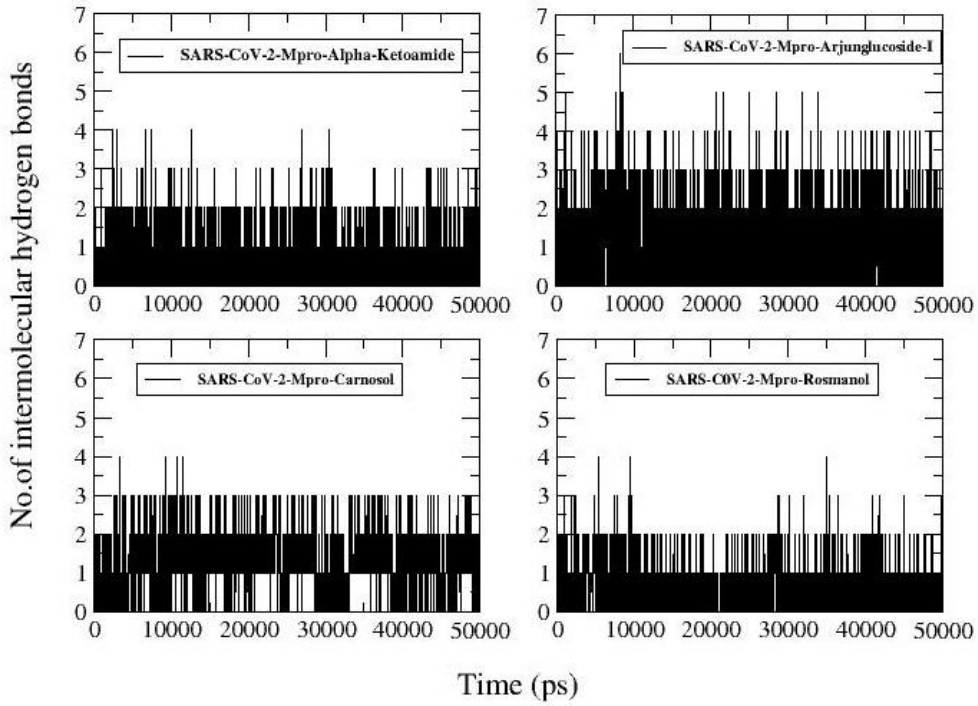

Figure 6. The number of intermolecular hydrogen bonds between SARS-CoV-2 Mpro and the small molecule inhibitors as a function of simulation time in picoseconds.

3.5. Binding free energy (BFE) and per residue energy decomposition (PRED) analysis.

The molecular mechanic energies were integrated using the MM-PBSA/GBSA method to further study the free energy of the binding of small molecules with the SARS-CoV-2 Mpro. Because MM-PBSA/GBSA approach uses a continuum solvent technique to determine the binding free energies of a complex system, the binding energy values here represent the relative binding free energy, not the absolute or total binding free energy. The main goal of these methods is to determine the difference in free energy between the bound and unbound states of protein-ligand complexes. The MM-PBSA/GBSA approach was used to calculate all of the thermochemical characteristics by using the AMBER suite for each coordinate at every 10 ps sampling frequency throughout the MD trajectory for all of the protein-ligand complexes. The most stable complexes were considered to be those with the lowest binding energy. The binding free energy analysis for SARS-CoV-2 Mpro- small molecule inhibitor complexes were tabulated in detail in Supplementary (Tables S9-S16), and the summary of the findings was presented in (Table 3) (MM-GBSA) and (Table 4) (MM-PBSA). The total free energies (ΔG_{bind}) obtained from MM-GBSA, and MM-PBSA for the protein-ligand complexes show comparable values (-13.14 kcal mol^{-1} from MM-GBSA and -5.31 kcal mol^{-1} from MM-PBSA for the SARS-CoV-2 Mpro-Alpha-ketoamide complex, -19.74 kcal mol^{-1} from MM-GBSA and -9.13 kcal mol^{-1} from MM-PBSA for the SARS-CoV-2 Mpro-Arjunglucoside-I complex, -16.81 kcal mol^{-1} from MM-GBSA and -9.98 kcal mol^{-1} from MM-PBSA for the SARS-CoV-2 Mpro-Carnosol complex, -14.05 kcal mol^{-1} from MM-GBSA and -5.87 kcal mol^{-1} from MM-PBSA for the SARS-CoV-2 Mpro-Rosmanol complex). ΔG_{bind} showed the least value for the SARS-CoV-2 Mpro and Arjunglucoside-I complex, followed by SARS-CoV-2 Mpro-Carnosol complex, SARS-CoV-2 Mpro-Rosmanol

complex, and SARS-CoV-2 Mpro-Alpha-ketoamide complex. These findings point to these small molecules derived from Indian spices as potential SARS-CoV-2 Mpro inhibitors.

Table 3. Binding Free Energy analysis for SARS-CoV-2 main protease(Mpro) –small molecule inhibitor complexes using Molecular Mechanics-Generalized Borne Surface Area (MM-GBSA) approach.

S.No.	Name of the Complex	▲G_{GBTOT} (kcal/mol)	▲G_{TSTOT} (kcal/mol)	▲G_{bind} (kcal/mol)
1.	SARS-CoV-2 Mpro-AKA complex	-35.90	-22.76	-13.14
2.	SARS-CoV-2 Mpro–AR complex	-40.39	-20.65	-19.74
3.	SARS-CoV-2 Mpro-CAN complex	-34.93	-18.12	-16.81
4.	SARS-CoV-2 Mpro-ROS complex	-34.19	-20.14	-14.05

Final estimated binding free energy (▲G_{GBTOT}); total entropic contribution (▲G_{TSTOT}); binding free energy (▲G_{bind}).

Table 4. Binding Free Energy analysis for SARS-CoV-2 main protease(Mpro) –small molecule inhibitor complexes using Molecular Mechanics-Generalized Borne Surface Area (MM-PBSA) approach.

S.No.	Name of the Complex	▲G_{PBTOT} (kcal/mol)	▲G_{TSTOT} (kcal/mol)	▲G_{bind} (kcal/mol)
1.	SARS-CoV-2 Mpro-AKA complex	-28.07	-22.76	-5.31
2.	SARS-CoV-2 Mpro–AR complex	-29.78	-20.65	-9.13
3.	SARS-CoV-2 Mpro-CAN complex	-28.10	-18.12	-9.98
4.	SARS-CoV-2 Mpro-ROS complex	-26.01	-20.14	-5.87

final estimated binding free energy (▲G_{PBTOT}); total entropic contribution ▲ (G_{TSTOT}); binding free energy (▲G_{bind}).

3.6. The decomposition of residue.

To better understand the protein-ligand binding mechanism, the contribution of each individual residue to the binding free energy has been studied in depth. To construct the residue-ligand interaction spectrum, the binding free energy is decomposed in terms of interacting residue-ligand pairs., shown in Supplementary (Figures S12-S15). The method of residue decomposition is particularly useful for explaining the protein-ligand binding mechanism at the atomic level and analyzing each residue's contribution to the binding free energy. The contribution toward binding free energy of several key residue-ligand pairs is split into vdW energy, the sum of electrostatic energy and polar solvation energy, and non-polar solvation energy, according to the analytic result residue-ligand interaction spectrum. The results have been depicted in Supplementary (Figures S12-S15). From the analysis, we can see the residues in the binding pocket of SARS-CoV-2 Mpro make a significant contribution to binding free energy

4. Conclusions

This study found that small molecule inhibitors (Carnosol, Arjunglucoside-I, and Rosmanol) from Indian spices can act as possible SARS-CoV-2 Mpro inhibitors. We used an in silico approach to conducting research in this regard. Our findings suggested that Arjunglucoside-I inhibits the SARS-CoV-2 Mpro the most, followed by Carnosol, Rosmanol, and then Alpha-

ketoamide (positive control). The PMF calculations revealed that the small molecule inhibitors have a deeper energy potential depth and, consequently, a longer residence period (Arjunglucoside-I, Carnosol, and Rosmanol) in the binding pocket SARS-CoV-2 Mpro. The order of inhibition among the small molecule inhibitors and Alpha-ketoamide (positive control) was determined using binding free energy calculations. ΔGbind showed the least value for the SARS-CoV-2 Mpro and Arjunglucoside-I complex, followed by SARS-CoV-2 Mpro-Carnosol complex, SARS-CoV-2 Mpro-Rosmanol complex, and SARS-CoV-2 Mpro-Alpha-ketoamide complex. These findings point to small molecule inhibitors derived from Indian spices as potential SARS-CoV-2 Mpro inhibitors. From the PRED analysis, we found the residues present in the binding pocket of SARS-CoV-2 Mpro have a major contribution to the total binding energy for the SARS-CoV-2 Mpro-small molecules interactions. Our findings shed light on the binding pathway and degree of association between SARS-CoV-2 Mpro and the small molecules (Arjunglucoside-I, Carnosol, and Rosmanol, Alpha-ketoamide (positive control)) in the complex formation. These findings could aid in the development of novel SARS-CoV-2 Mpro inhibitors.

Funding

This research received no external funding.

Acknowledgments

The authors extend their deepest gratitude to Tezpur University and University Grants Commission, India, for the start-up grant.

Conflicts of Interest

The authors declare no conflict of interest.

References

1. Cucinotta, D.; Vanelli, M. WHO declares COVID-19 a pandemic. *Acta Biomed* **2020**, *91*, 157–160, https://doi.org/10.23750/abm.v91i1.9397.
2. Touret, F.; Gilles, M.; Barral, B.; Nougairède, A.; Decroly, E.; Lamballerie, X.D.; Coutard, B. In vitro screening of a FDA approved chemical library reveals potential inhibitors of SARS-CoV-2 replication. *Scientific Reports* **2020**, *10*, 13093, https://doi.org/10.1038/s41598-020-70143-6.
3. Kickbusc, I.; Leun, G. Response to the emerging novel coronavirus outbreak. *BMJ* **2020,** 368, https://doi.org/10.1136/bmj.m406.
4. Banerjee, A.; Kulcsar, K.; Misra, V.; Frieman, M.; Mossman, K. Bats and coronaviruses. *Viruses* **2019**, *11*, 41, https://dx.doi.org/10.3390%2Fv11010041.
5. Yang, D.; Leibowitz, J.L. The structure and functions of coronavirus genomic 3′ and 5′ ends. *Virus Res.* **2015**, *206*, 120–133, https://doi.org/10.1016/j.virusres.2015.02.025.
6. Ward, M.P.; Li. X.; Tian, K. Novel coronavirus 2019, an emerging public health emergency. *Transbound Emerg. Dis.* **2020**, *67*, 469-470, https://doi.org/10.1111/tbed.13509.
7. Paules, C.I.; Marston, H.D.; Fauci, A.S. Coronavirus Infections-More than Just the Common Cold. *JAMA* **2020**, *6*, 476-477, https://doi.org/10.1001/jama.2020.0757.
8. Krausslich, H.G.; Wimmer, E. Viral proteinases. *Annual Review Biochem.* **1988**, *57*, 701–754, https://doi.org/10.1146/annurev.bi.57.070188.003413.
9. Tong, L. Viral proteases. *Chem. Rev.* **2002**, *102*, 4609–4626, https://doi.org/10.1021/cr010184f.

10. Mengist, H.M.; Dilnessa, T.; Jin, T. Structural Basis of Potential Inhibitors Targeting SARS-CoV-2 Main Protease. *Front. Chem*. **2021,** *9*, 622898, https://doi.org/10.3389/fchem.2021.622898.
11. Citarella, A.; Scala, A.; Piperno, A.; Micale, N. SARS-CoV-2 M^{pro}: A Potential Target for Peptidomimetics and Small-Molecule Inhibitors. *Biomolecules* **2021**, *11*, 607, https://doi.org/10.3390/biom11040607.
12. Huff,S.; Kummetha,I.R.;Tiwari, S.K.; Huante,M.B.; Clark,A.E.; Wang,S.; Bray,W.; Smith,D.; Carlin,A.F.; Endsley,M.; Rana,T.M. Discovery and Mechanism of SARS-CoV-2 Main Protease Inhibitors. *J. Med. Chem.* 2022, 65, 4, 2866–2879, https://doi.org/10.1021/acs.jmedchem.1c00566.
13. Krumm, Z.A.; Lloyd, G.M.; Francis, C.P.; Nasif, L.H.; Mitchell, D.A.; Golde, T.E.; Giasson, B.I.; Xia, Y. Precision therapeutic targets for COVID-19. *Viro. J.* **2021**, *18*, 66, https://doi.org/10.1186/s12985-021-01526-y.
14. Li, J.Q.; Gao, H.; Zhai, L.; Sun, L.Y.; Chen, C.; Chigan, J.Z.; Ding, H.H.; Yang, K.W. Dipyridyl-substituted thiosemicarbazone as a potent broad-spectrum inhibitor of metallo-β-lactamases. *Bioorg Med Chem.* **2021**, 38,116128, https://doi.org/10.1016/j.bmc.2021.116128.
15. Gossen, J.; Albani, S.; Hanke, A.; Joseph, B.P.; Bergh, C.; Kuzikov, M.; Costanzi, E.; Manelfi, C.; Storici, P.; Gribbon, P.; Beccari, A.R.; Talarico, C.; Spyrakis, F.; Lindahl, E.; Zaliani, A.; Carloni, P.; Wade, R.C.; Muziani, F.; Kokh, D.B.; Rossetti, G. A Blueprint for High Affinity SARS-CoV-2 Mpro Inhibitors from Activity-Based Compound Library Screening Guided by Analysis of Protein Dynamics. *ACS Pharmacol. Transl. Sci*. **2021**, *4*, 1079–1095, https://doi.org/10.1021/acsptsci.0c00215.
16. Sharma, A.; Vora, J.; Patel, D.; Sinha, S.; Jha, P.C., Shrivastava, N. Identification of natural inhibitors against prime targets of SARS-CoV-2 using molecular docking, molecular dynamics simulation and MM-PBSA approaches. *J. Biomol. Struct. Dyn.* **2022**, *40*, 3296-3311, https://doi.org/10.1080/07391102.2020.1846624.
17. Liu, J.; Zhu, J.; Xue, J.; Qin, Z.; Shen, F.; Liu, J.; Chen, X.; Li, X.; Wu, Z.; Xiao, W.; Zheng, C.; Wang, Y. In silico-based screen synergistic drug combinations from herb medicines: a case using Cistanche tubulosa. *Sci. Rep.* **2017,** *7*, 16364, https://doi.org/10.1038/s41598-017-16571-3.
18. Rahimi, A.; Mirzazadeh, A.; Tavakolpour, S. Genetics and genomics of SARS-CoV-2: A review of the literature with the special focus on genetic diversity and SARS-CoV-2 genome detection. *Genomics* **2021**, *113*, 1221-1232, https://doi.org/10.1016/j.ygeno.2020.09.059.
19. Zhang, L.; Lin, D.; Sun, X.; Curth, U.; Drosten, C.; Sauerhering, L.; Becker, S.; Rox, K.; Hilgenfeld, R. Crystal structure of SARS-CoV-2 main protease provides a basis for design of improved α-ketoamide inhibitors. *Science* **2020**, *368*, 409–412, https://doi.org/10.1126/science.abb3405.
20. Morse, J.S.; Lalonde, T.; Xu, S.; Liu, W.R. Learning from the Past: Possible Urgent Prevention and Treatment Options for Severe Acute Respiratory Infections Caused by 2019-nCoV. *Chembiochem*. **2020**, *21*, 730–738, https://doi.org/10.1002/cbic.202000047.
21. Sk, M.F.; Roy, R.; Kar, P. Exploring the potency of currently used drugs against HIV-1 protease of subtype D variant by using multiscale simulations. *J. Biomol. Struct. Dyn.* **2020**, *39*, 3649-3661, https://doi.org/10.1080/07391102.2020.1724196.
22. Cui, W.; Yang, K.; Yang, H. Recent Progress in the Drug Development Targeting SARS-CoV-2 Main Protease as Treatment for COVID-19. *Front. Mol. Biosci.* **2020**, *7*, 616341, https://doi.org/10.3389/fmolb.2020.616341.
23. Abdellatiif, M. H.; Ali, A.; Ali, A.; Hussien, M. Computational studies by molecular docking of some antiviral drugs with COVID-19 receptors are an approach to medication for COVID-19. *Open Chem.* **2021**, *19*, 245-264, https://doi.org/10.1515/chem-2021-0024.
24. Muralidharan, N.; Sakthivel, R.; Velmurugan, D.; Gromiha, M.M. Computational studies of drug repurposing and synergism of lopinavir, oseltamivir and ritonavir binding with SARS-CoV-2 protease against COVID-19. *J. Biomol. Struct. Dyn.* **2021,** *39*, 2673-2678, http://doi.org/10.1080/07391102.2020.1752802.
25. Mongia, A.; Saha, S.K.; Chouzenoux, E.; Majumdar, A. A computational approach to aid clinicians in selecting antiviral drugs for COVID-19 trials. *Sci. Rep.* **2021**, *11*, 9047, https://doi.org/10.1038/s41598-021-88153-3.
26. Behera, S.K.; Vhora, N.; Contractor, D.; Shard, A.; Kumar, D.; Kalia, K.; Jain. A. Computational drug repurposing study elucidating simultaneous inhibition of entry and replication of novel corona virus by Grazoprevir. *Sci. Rep.* **2021**, *11*, 7307, https://doi.org/10.1038/s41598-021-86712-2.
27. Egieyeh, S.; Egieyeh, E.; Malan, S.; Christofells, A.; Fielding, B. Computational drug repurposing strategy predicted peptide-based drugs that can potentially inhibit the interaction of SARS-CoV-2 spike protein with its target (humanACE2). *PLoS ONE* **2021**, *16*, e0245258, https://doi.org/10.1371/journal.pone.0245258.

28. Coban, M.A.; Morrison, J.; Maharjan, S.; Medina, D.H.H.; Li, W.; Zhang, Y.S.; Freeman, W.D.; Radisky, E.S.; Le Roche, K.G.; Weisend, C.M.; Ebihara, H.; Caulfield, T.R. Attacking COVID-19 progression using multi-drug therapy for synergetic target engagement. *Biomolecules* **2021**, *11*, 787, http://doi.org/10.3390/biom11060787.
29. Basak, S.C.; Kier, L.B. COVID-19 pandemic: how can computer-assisted methods help to rein in this global menace? *Curr. Comput.-Aided Drug Des.* **2021**, *17*, http://dx.doi.org/10.2174/1573409917012101121032l5.
30. Ibrahim, M.A.A.; Abdelrahman, A.H.M.; Allemailem, K.S.; Almatroudi, A.; Moustafa, M.F.; Hegazy, M.E.F. In silico evaluation of prospective anti-COVID-19 drug candidates as potential SARS-CoV-2 main protease inhibitors. *Protein J.* **2021**, *40*, 296-309, https://doi.org/10.1007/s10930-020-09945-6.
31. Singh, S.K.; Upadhyay, A.K.; Reddy, M.S. Screening of potent drug inhibitors against SARS-CoV-2 RNA polymerase: an in silico approach. *3 Biotech* **2021**, *11*, 93, http://doi.org/10.1007/s13205-020-02610-w.
32. Enmozhi, S.K.; Raja, K.; Sebastine, I.; Joseph, J. Andrographolide as a potential inhibitor of SARS-CoV-2 main protease: an in silico approach. *J. Biomol. Struct. Dyn.* **2021**, *39*, 3092–3098, http://doi.org/10.1080/07391102.2020.1760136.
33. Mahanta, S.; Chowdhury, P.; Gogoi, N.; Goswami, N.; Borah, D.; Kumar, R.; Chetia, D.; Borah, P.; Buragohain, A.K.; Gogoi, B. Potential antiviral activity of approved repurposed drug against main protease of SARS-CoV-2: an in silico based approach. *J. Biomol. Struct. Dyn.* **2021**, *39*, 3802–3811, https://doi.org/10.1080/07391102.2020.1768902.
34. Beura, S.; Chetti, P. In-silico strategies for probing chloroquine based inhibitors against SARS-CoV-2. *J. Biomol. Struct. Dyn*. **2021**, *39*, 3747–3759, http://doi.org/10.1080/07391102.2020.1772111.
35. Mittal, L.; Kumari, A.; Srivastava, M.; Singh, M.; Asthana, S. Identification of potential molecules against COVID-19 main protease through structure-guided virtual screening approach. *J. Biomol. Struct. Dyn*. **2021**, *39*, 3662–3680, http://doi.org/10.1080/07391102.2020.1768151.
36. Wahedi, H.M.; Ahmad, S.; Abbasi, S.W. Stilbene-based natural compounds as promising drug candidates against COVID-19. *J. Biomol. Struct. Dyn*. **2021**, *39*, 3225–3234, http://doi.org/10.1080/07391102.2020.1762743.
37. Selvaraj, C.; Dinesh, D.C.; Panwar, U.; Abhirami, R.; Boura, E.; Singh, S.K. Structure-based virtual screening and molecular dynamics simulation of SARS-CoV-2 guanine-N7 methyltransferase (nsp 14) for identifying antiviral inhibitors against COVID-19. *J. Biomol. Struct. Dyn*. **2021**, *39*, 4582-4593, http://doi.org/10.1080/07391102.2020.1778535.
38. Hassab, M.A.E.; Ibrahim, T.M.; Al-Rashood, S.T.; Alharbi, A.; Eskandrani, R.O.; Eldehna, W.M. In silico identification of novel SARS-COV-2 2-O-methyltransferase (nsp16) inhibitors: structure-based virtual screening, molecular dynamics simulation and MM-PBSA approaches. *J. Enzyme Inhib. Med. Chem* **2021**, *36*, 727–736, http://doi.org/10.1080/14756366.2021.1885396.
39. Elmaaty, A.A.; Darwish, K.M.; Khattab, M.; Elhady, S.S.; Salah, M.; Hamed, M.I.A.; Al-Karmalawy, A.A.; Saleh, M.M. In a search for potential drug candidates for combating COVID-19: computational study revealed salvianolic acid B as a potential therapeutic targeting 3CLpro and spike proteins. *J. Biomol. Struct. Dyn*. **2021**, 1-28, https://doi.org/10.1080/07391102.2021.1918256.
40. Al-Karmalawy, A.; Dahab, M.; Metwaly, A.; Elhadi, S.S.; Elkaeed, E.B.; Eissa, I.H.; Darwish, K.M. Molecular docking and dynamics simulations reveal the potential of anti-HCV drugs to inhibit COVID-19 main protease. *Front Chem* **2021**, *9*, 661230, https://doi.org/10.3389/fchem.2021.661230.
41. Sharanya, C.S.; Sabu, A.; Haridas, M. Potent phytochemicals against COVID-19 infection from phyto-materials used as antivirals in complementary medicines: a review. *Futur. J. Pharm. Sci.* **2021**, *7*, 113, https://doi.org/10.1186/s43094-021-00259-7.
42. Nabi, F.; Ahmad, O.; Khan, Y.A.; Nabi, A.; Amiruddin, H.M.; Qais, F.A.; Masroor, A.; Hisamuddin, M.; Uversky, V.N.; Khan, R.H. Computational studies on phylogeny and drug designing using molecular simulations for COVID-19. *J. Biomol. Struct. Dyn*. **2021**, 1-10, http://doi.org/10.1080/07391102.2021.1947895.
43. Umesh; Kundu, D.; Selvaraj, C.; Singh, S.K.; Dubey, V.K. Identification of new anti-nCoV drug chemical compounds from Indian spices exploiting SARS-CoV-2 main protease as target. *Journal of biomolecular structure and dynamics* **2021**, *39*, 3428-3434, https://doi.org/10.1080/07391102.2020.1763202.
44. Cui, W.; Yang, K.; Yang , H. Recent Progress in the Drug Development Targeting SARS-CoV-2 Main Protease as Treatment for COVID-19. *Front.Mol.Biosci*. **2020**, *7*, https://doi.org/10.3389/fmolb.2020.616341.

45. Alsamri, H.; Hasasna, H.E.; Baby, B.; Alneyadi, A.; Dhaheri, Y.A.; Ayoub, M.A.; Eid, A.H.; Vijayan, R.; Iratni, R. Carnosol Is a Novel Inhibitor of p300 Acetyltransferase in Breast Cancer. *Front. Oncol.* **2021**, *11*, 664403, https://doi.org/10.3389/fonc.2021.664403.
46. Lo, A.H.; Liang, Y.C.; Shiau, S.Y.L.; Ho, C.T.; Lin, J.K. Carnosol, an antioxidant in rosemary, suppresses inducible nitric oxide synthase through down-regulating nuclear factor-κB in mouse macrophages. *Carcinogenesis* **2002**, *23*, 983–991, https://doi.org/10.1093/carcin/23.6.983.
47. Berman, H.M.; Westbrook, J.; Feng, Z.; Gilliland, G.; Bhat, T.N.; Weissig, H.; Shindyalov, I.N.; Bourne, P.E. The protein data bank. *Nucl. Acids Res.* **2000**, *28*, 235-242, https://doi.org/10.1093/nar/28.1.235.
48. Duhovny, D.; Nussinov, R.; Wolfson, H.J. Efficient Unbound Docking of Rigid Molecules. In: *Guigó, R., Gusfield, D. (eds) Algorithms in Bioinformatics. WABI* **2002**. *Lecture Notes in Computer Science* vol 2452, Springer, Berlin, Heidelberg, https://doi.org/10.1007/3-540-45784-4_14.
49. Connolly, M.L. Analytical molecular surface calculation. *J. Appl. Crystallogr.* **1983**, *16*, 548–558, https://doi.org/10.1107/S0021889883010985.
50. Connolly M.L. Solvent-accessible surfaces of proteins and nucleic acids. *Science* **1983**, *221*, 709–713, https://doi.org/10.1126/science.6879170.
51. Pettersen, E.F.; Goddard, T.D.; Huang, C.C.; Couch, G.S.; Greenblatt, D.M.; Meng, E.C.; Ferrin, T.E. UCSF Chimera? A visualization system for exploratory research and analysis. *J. of Comp. Chem.* **2004**, *25*, 1605−1612, https://doi.org/10.1002/jcc.20084.
52. Jorgensen, W.L.; Chandrasekhar, J.; Madura, J.D.; Impey, R.W.; Klein, M.L. Comparison of simple potential functions for simulating liquid water. *J. Chem. Phys.* **1983**, *79*, 926−935, http://dx.doi.org/10.1063/1.445869.
53. Darden, T.; York, D.; Pedersen, L. Particle mesh Ewald: An N· log (N) method for Ewald sums in large systems. *J. Chem. Phys.* **1993**, *98*, 10089-10092, https://doi.org/10.1063/1.464397.
54. Salomon-Ferrer, R.; Gotz, A.W.; Poole, D.; Le Grand, S.; Walker, R.C. Routine microsecond molecular dynamics simulations with AMBER on GPUs. 2. Explicit solvent particle mesh Ewald. *J. Chem. Theory Comput.* **2013**, *9*, 3878-3888, https://doi.org/10.1021/ct400314y.
55. Ryckaert, J.P.; Ciccotti, G.; Berendsen, H.J.C. Numerical integration of the cartesian equations of motion of a system with constraints: molecular dynamics of n-alkanes. *J. Comp. Phys.* **1977**, *23*, 327−341, https://doi.org/10.1016/0021-9991(77)90098-5.
56. Berendsen, H.J.; Postma, J.V.; Van, G.W.F.; DiNola, A.R.H.J.; Haak, J.R. Molecular dynamics with coupling to an external bath. *J. Chem. Phys.* **1984**, *81*, 3684-3690, https://doi.org/10.1063/1.448118.
57. Roux, B. The calculation of the potential of mean force using computer simulations. *Comp. Phys. Comm.* **1995**, *91*, 275−282, https://doi.org/10.1016/0010-4655(95)00053-I.
58. Kumar, S.; Rosenberg, J.M.; Bouzida, D.; Swendsen, R.H.; Kollman, P.A. The weighted histogram analysis method for freeenergy calculations on biomolecules. I. The method. *J. Comp. Chem.* **1992**, *13*, 1011−1021, https://doi.org/10.1002/jcc.540130812.
59. Souaille, M.; Roux, B. Extension to the weighted histogram analysis method: combining umbrella sampling with free energy calculations. *Comput. Phys. Commun.* **2001**, *135*, 40−57, https://doi.org/10.1016/s0010-4655(00)00215-0.
60. Roe, D.R.; Cheatham III, T.E. PTRAJ and CPPTRAJ: software for processing and analysis of molecular dynamics trajectory data. *J. Chem. Theor. Comp.* **2013**, *9*, 3084−3095, https://doi.org/10.1021/ct400341p.
61. Miller III, B.R.; McGee Jr, T.D.; Swails, J.M.; Homeyer, N.; Gohlke, H.; Roitberg, A.E. MMPBSA.py: an efficient program for end-state free energy calculations. *J. Chem. Theor. Comp.* **2012**, *8*, 3314-3321, https://doi.org/10.1021/ct300418h.
62. Chen, F.; Liu, H.; Sun, H.; Pan, P.; Li, Y.; Li, D.; Hou, T. Assessing the performance of the MM/PBSA and MM/GBSA methods. 6. Capability to predict protein–protein binding free energies and re-rank binding poses generated by protein–protein docking. *Phys. Chem. Chem. Phys.* **2016**, *18*, 22129-22139, https://doi.org/10.1039/c6cp03670h.
63. Genheden, S.; Ryde, U. The MM/PBSA and MM/GBSA methods to estimate ligand-binding affinities. *Exp. Opin. Drug Dis.* **2015**, *10*, 449-461, http://doi.org/10.1517/17460441.2015.1032936.
64. Case, D.A. Normal mode analysis of protein dynamics. *Curr. Opin. Struc. Bio.* **1994**, *4*, 285-290, https://doi.org/10.1016/S0959-440X(94)90321-2.

65. Karplus, M.; Kushick, J.N. Method for estimating the configurational entropy of macromolecules. *Macromol*. **1981**, *14*, 325-332, https://doi.org/10.1021/ma50003a019.
66. Chen, J.; Yin, B.; Pang, L.; Wang, W.; Zhang, J.Z.; Zhu, T. Binding modes and conformational changes of FK506-binding protein 51 induced by inhibitor bindings: insight into molecular mechanisms based on multiple simulation technologies. *J. Bio. Struc. Dyn*. **2020**, *38*, 2141-2155, https://doi.org/10.1080/07391102.2019.1624616.
67. Du, Q.; Qian, Y.; Yao, X.; Xue, W. Elucidating the tight-binding mechanism of two oral anticoagulants to factor Xa by using induced-fit docking and molecular dynamics simulation. *J. Bio. Struct. Dyn.* **2020**, *38*, 625-633, https://doi.org/10.1080/07391102.2019.1583605.
68. Sanabria-Chanaga, E.E.; Betancourt-Conde, I.; Hernandez-Campos, A.; Tellez-Valencia, A.; Castillo, R. *In silico* hit optimization toward AKT inhibition: fragment-based approach, molecular docking and molecular dynamics study. *J. Bio. Struc. Dyn.* **2019**, *37*, 4301-4311, http://doi.org/10.1080/07391102.2018.1546618.
69. Gao, J.; Wang, Y.; Chen, Q.; Yao, R. Integrating molecular dynamics simulation and molecular mechanics/generalized Born surface area calculation into pharmacophore modeling: a case study on the proviral integration site for Moloney murine leukemia virus (Pim)-1 kinase inhibitors. *J. Bio. Struc. Dyn*. **2020**, *38*, 581-588, http://doi.org/10.1080/07391102.2019.1571946.
70. Joshi, T.; Joshi, T.; Sharma, P.; Chandra, S.; Pande, V. Molecular docking and molecular dynamics simulation approach to screen natural compounds for inhibition of *Xanthomonas oryzae pv. Oryzae* by targeting Peptide Deformylase. *J. Bio. Struc. Dyn.* **2021**, *39*, 823-840, https://doi.org/10.1080/07391102.2020.1719200.
71. Sk, M.F.; Roy, R.; Kar, P. Exploring the potency of currently used drugs against HIV-1 protease of subtype D variant by using multiscale simulations. *J. Bio. Struct. Dyn.* **2021**, *39*, 988-1003, https://doi.org/10.1080/07391102.2020.1724196.
72. Sun, H.; Duan, L.; Chen, F.; Liu, H.; Wang, Z.; Pan, P.; Zhu, F.; Zhang, J.Z.H.; Hou, T. Assessing the performance of MM/PBSA and MM/GBSA methods. 7. Entropy effects on the performance of endpoint binding free energy calculation approaches. *Phys. Chem. Chem. Phys.* **2018**, *20*, 14450-14460, https://doi.org/10.1039/C7CP07623A.
73. Tian, S.; Ji, C.; Zhang, J.Z. Molecular basis of SMAC–XIAP binding and the effect of electrostatic polarization. *J. Bio. Struc. Dyn*. **2021**, *39*, 743-752, https://doi.org/10.1080/07391102.2020.1713892.
74. Wan, Y.; Guan, S.; Qian, M.; Huang, H.; Han, F.; Wang, S.; Zhang, H. Structural basis of fullerene derivatives as novel potent inhibitors of protein acetylcholinesterase without catalytic active site interaction: insight into the inhibitory mechanism through molecular modeling studies. *J. Bio. Struc. Dyn*. **2020**, *38*, 410-425, https://doi.org/10.1080/07391102.2019.1576543.
75. Wang, E.; Sun, H.; Wang, J.; Wang, Z.; Liu, H.; Zhang, J.Z.H.; Hou, T. End-Point Binding Free Energy Calculation with MM/PBSA and MM/GBSA: Strategies and Applications in Drug Design. *Chem. Rev*. **2019**, *119*, 9478- 9508, https://doi.org/10.1021/acs.chemrev.9b00055.
76. Zhang, W.; Yang, F.; Ou, D.; Lin, G.; Huang, A.; Liu, N.; Li, P. Prediction, docking study and molecular simulation of 3D DNA aptamers to their targets of endocrine disrupting chemicals. *J. Bio. Struc. Dyn*. **2019**, *37*, 4274-4282, https://doi.org/10.1080/07391102.2018.1547222.
77. Torrie, G.M.; Valleau, J.P. Monte Carlo study of a phase-separating liquid mixture by umbrella sampling. *J. Comput. Phys*. **1977**, *23*, 187−199, https://doi.org/10.1063/1.434125.
78. Sun, H.; Tian, S.; Zhou, S.; Li, Y.; Li, D.; Xu, L.; Shen, M.; Pan, P.; Hou, T. Revealing the favorable dissociation pathway of type II kinase inhibitors via enhanced sampling simulations and two-end-state calculations. *Sci. Rep.* **2015**, *5*, 8457, https://doi.org/10.1038/srep08457.

Supplementary Information

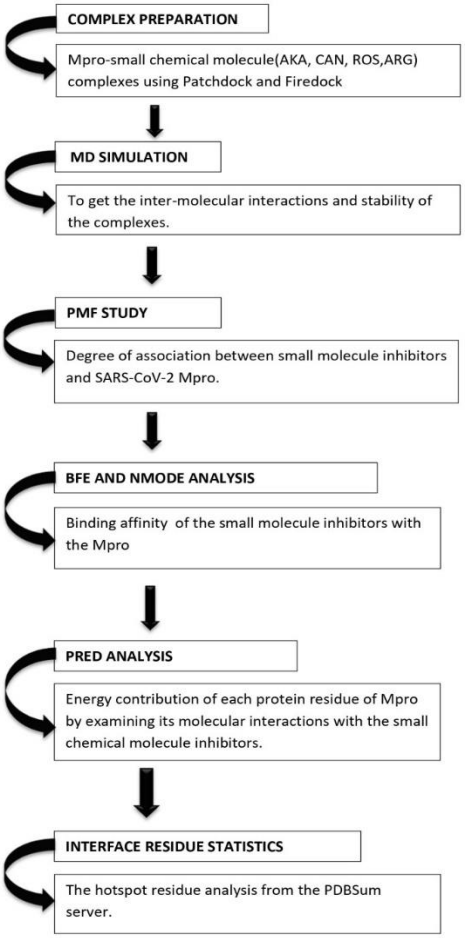

Figure S1. Flowchart represents the methods and protocols followed in this work.

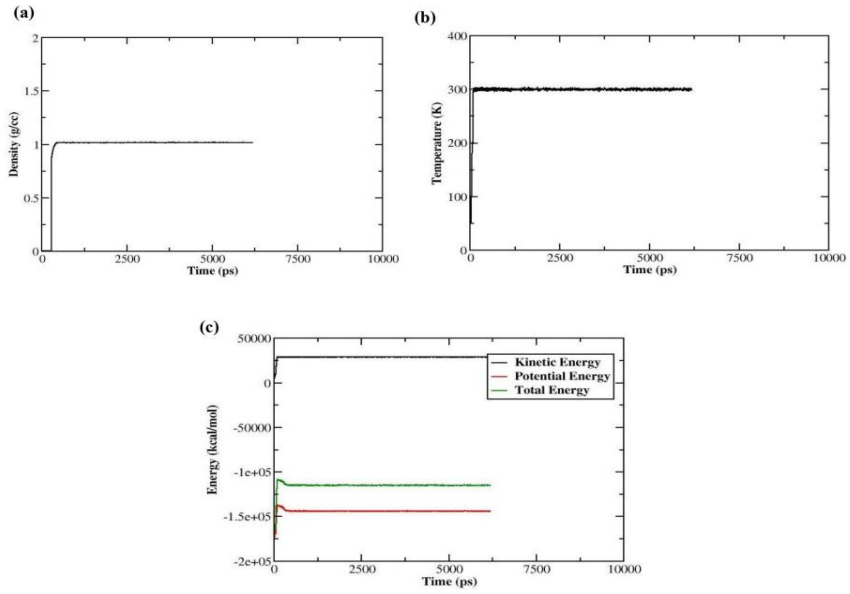

Figure S2. a) Density, b**)** Temperature, and c**)** Energy plots of SARS-CoV-2-Alpha-ketomaide complex system as a function of simulation time.

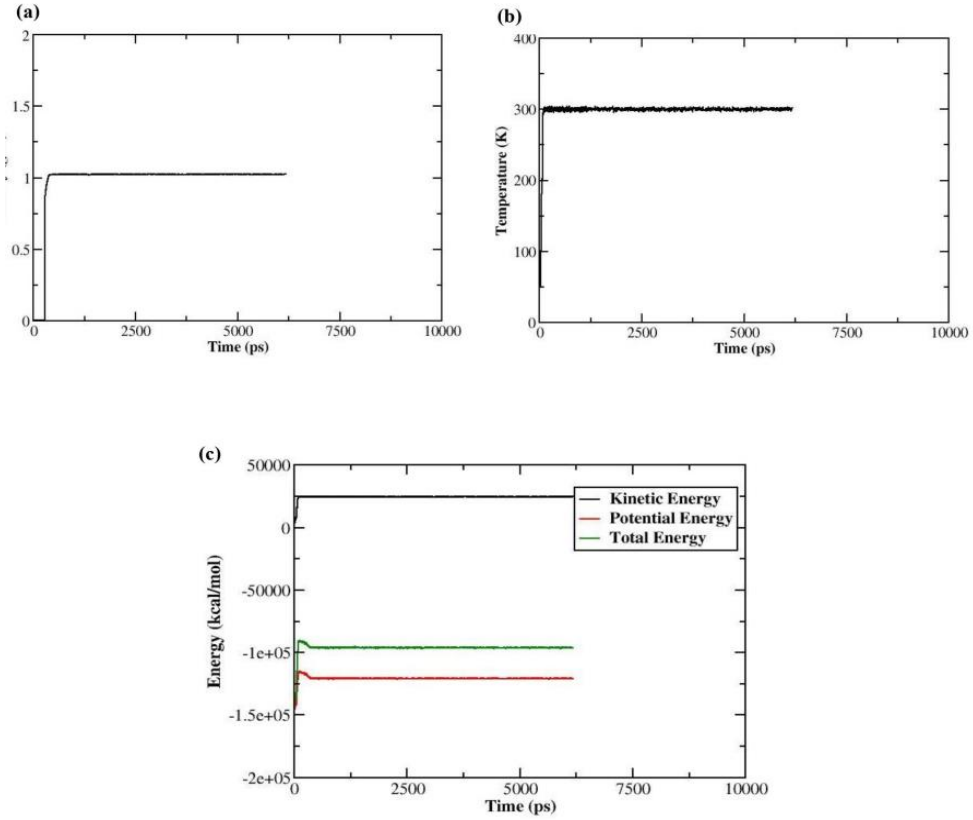

Figure S3. a) Density, b**)** Temperature and c**)** Energy plots of SARS-CoV-2-Arjunglucoside-I complex system as a function of simulation time.

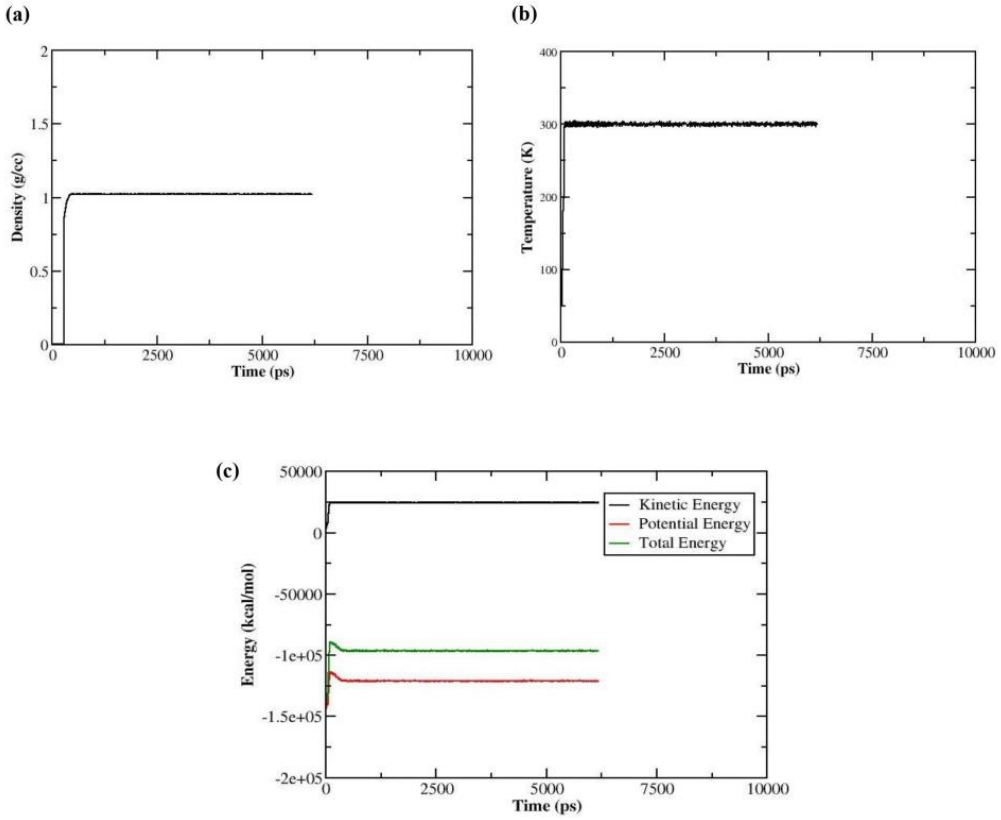

Figure S4. a) Density, b**)** Temperature, and c**)** Energy plots of SARS-CoV-2-Carnosol complex system as a function of simulation time.

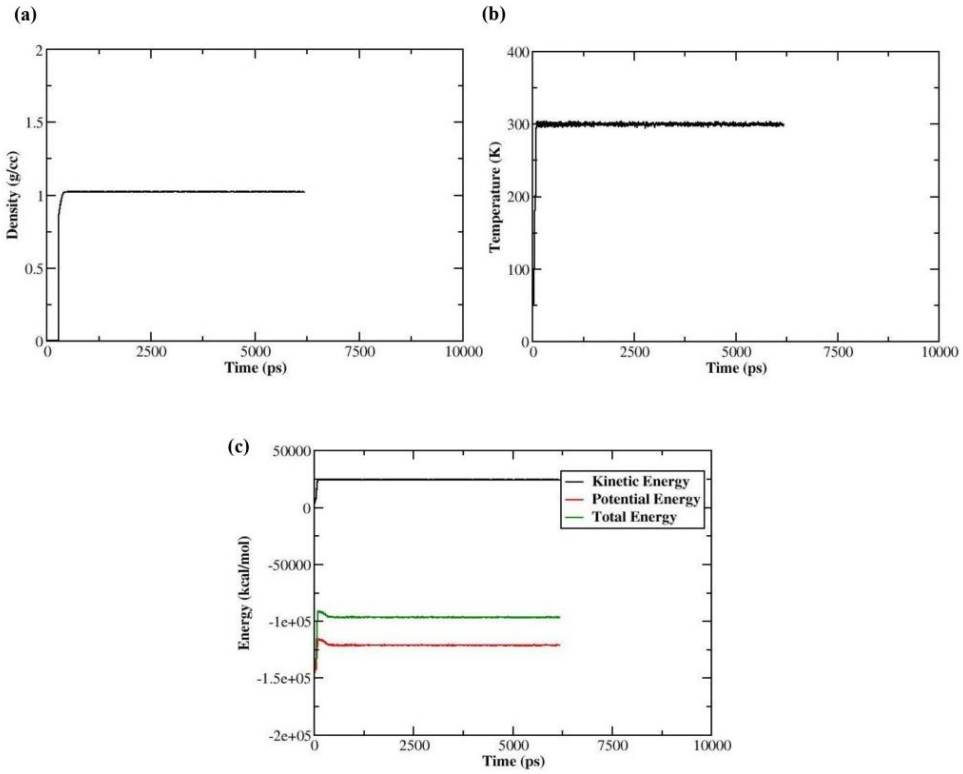

Figure S5. a) Density, b**)** Temperature, and c**)** Energy plots of SARS-CoV-2-Rosmanol complex system as a function of simulation time.

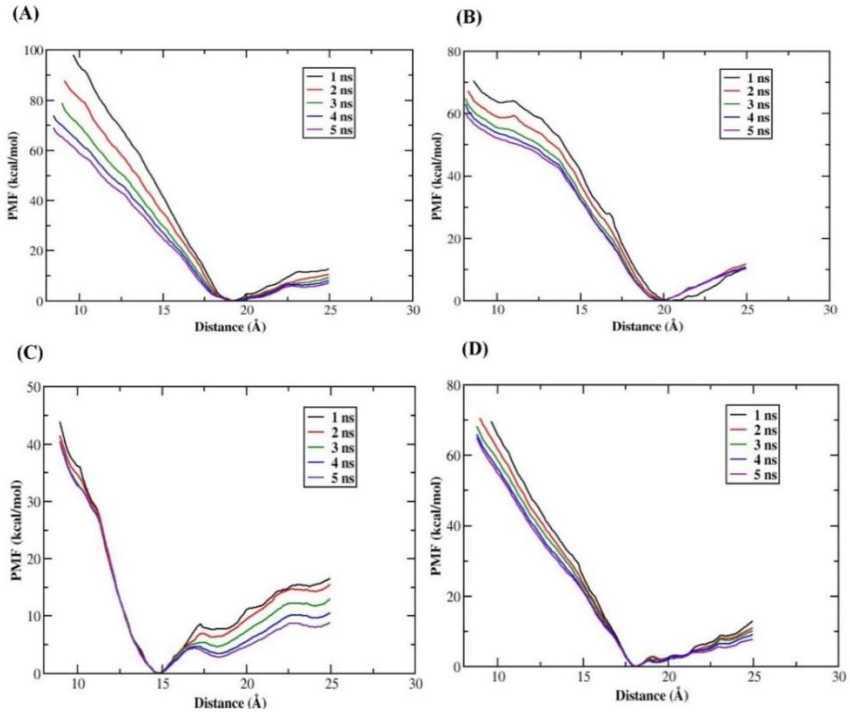

Figure S6. Convergence of the PMFs calculated by umbrella sampling for (A) SARS-CoV-2-Alpha-ketoamide (B) SARS-CoV-2-Arjunglucoside-I (C) SARS-CoV-2-Carnosol (D) SARS-CoV-2-Rosmanol complex where 5 ns US simulation were performed.

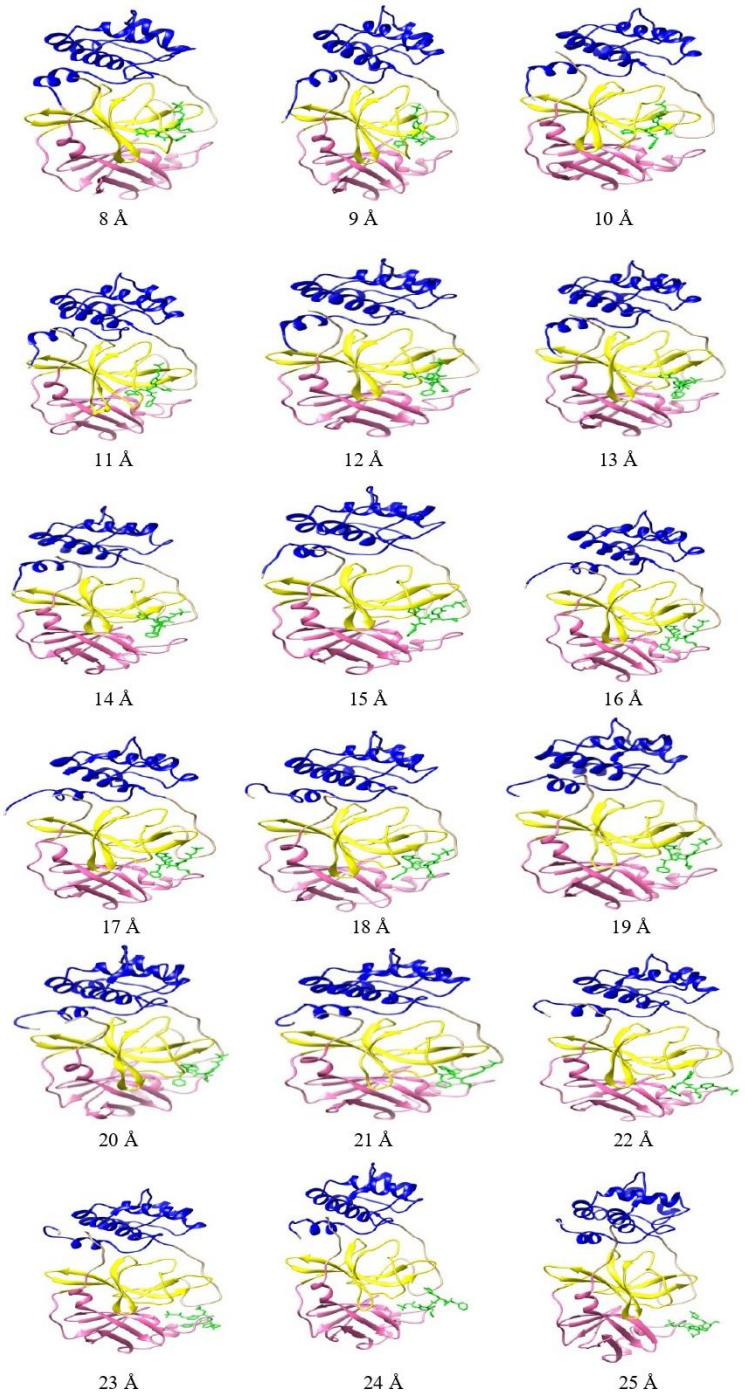

Figure S7. Snapshots of SARS-CoV-2 Mpro-Alpha-ketoamide complex structures at a discrete distance of separation (in Å) between their center of mass.

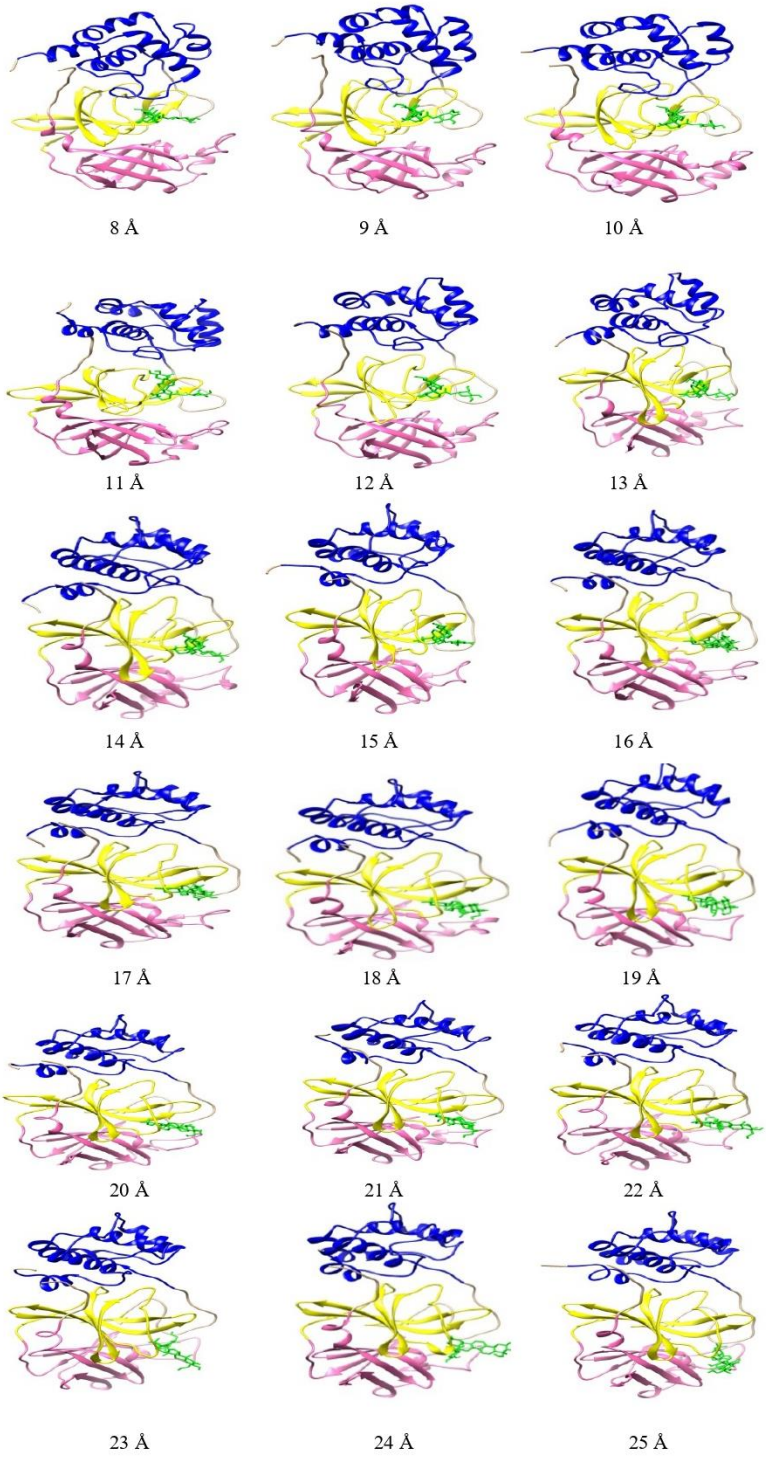

Figure S8. Snapshots of SARS-CoV-2 Mpro-Arjunglucoside-I complex structures at a discrete distance of separation (in Å) between their center of mass.

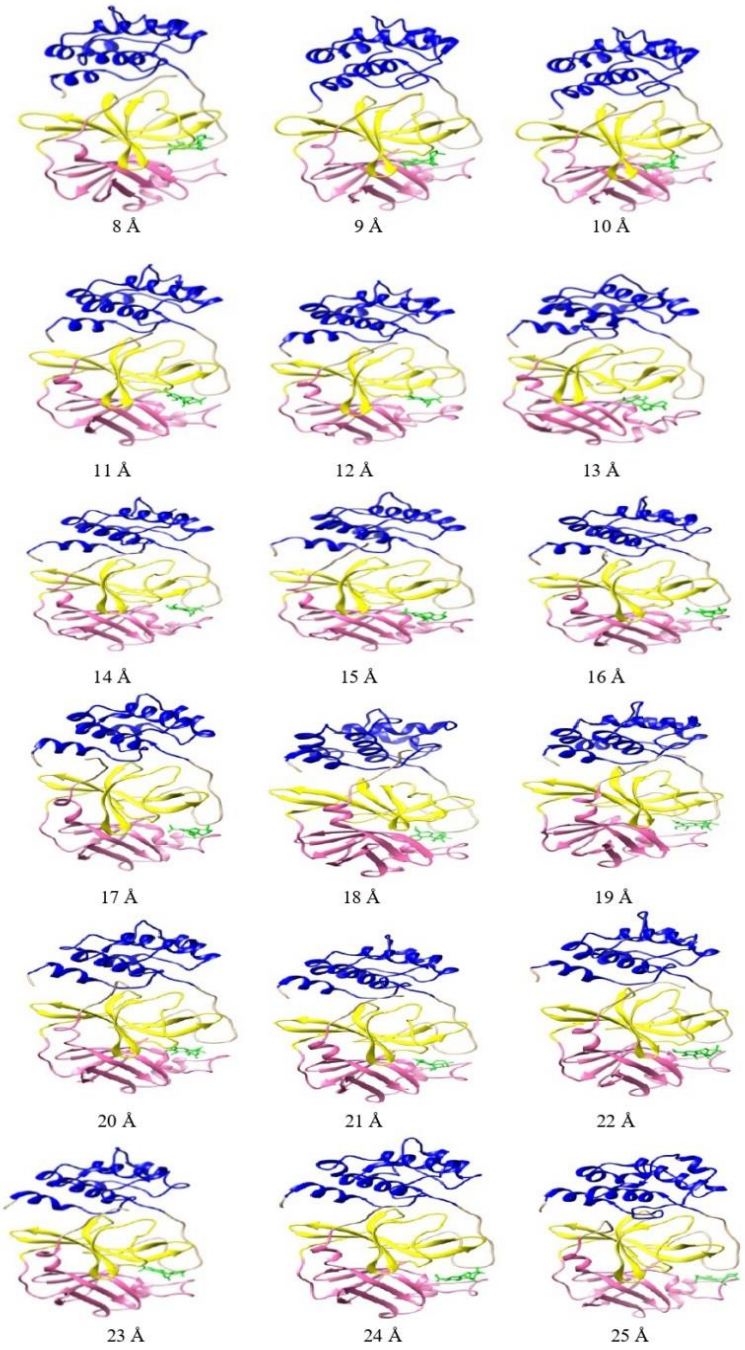

Figure S9. Snapshots of SARS-CoV-2 Mpro-Carnosol complex structures at a discrete separation distance (in Å) between their center of mass.

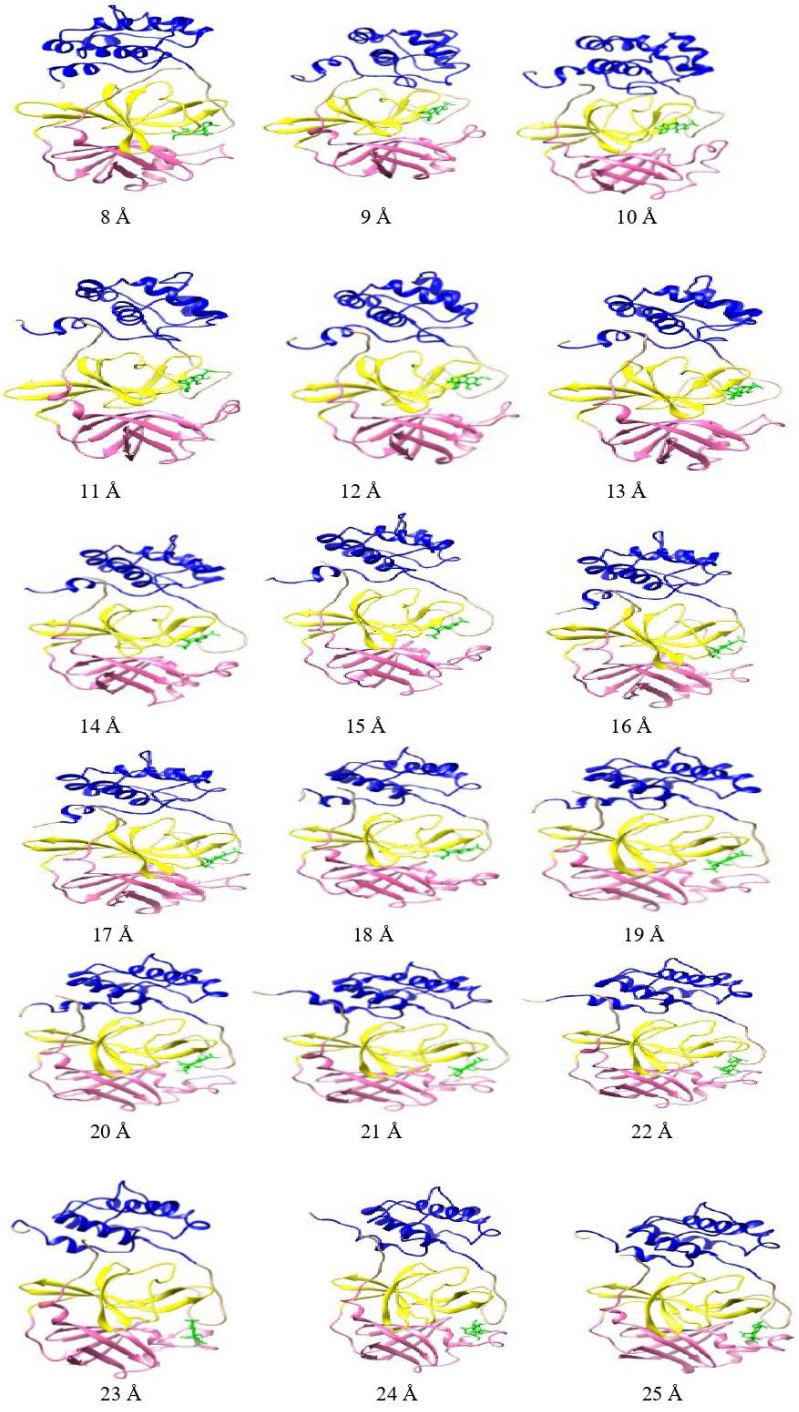

Figure S10. Snapshots of SARS-CoV-2 Mpro-Rosmanol complex structures at a discrete distance of separation (in Å) between their center of mass.

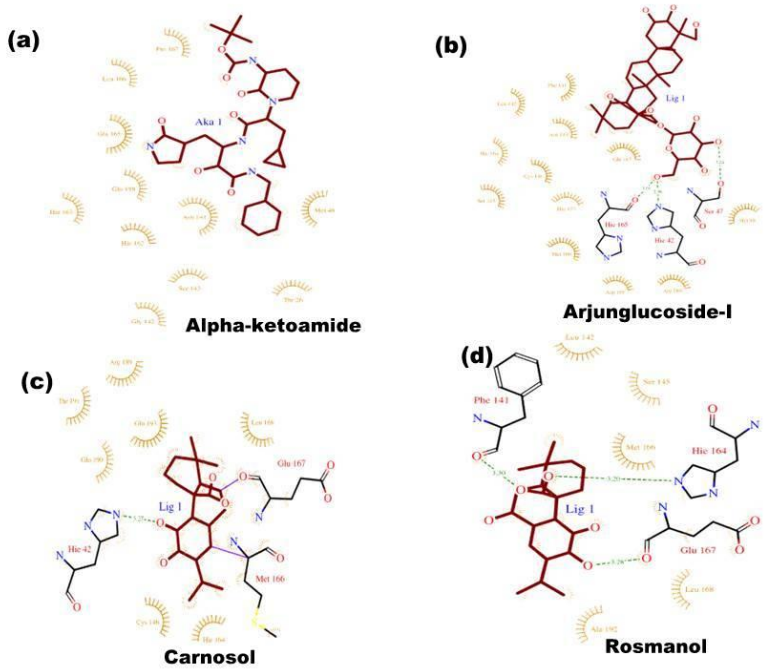

Figure S11. Amino acid residual interactions of the protein-ligand interface in (a) SARS-CoV-2-Alpha-ketoamide (b) SARS-CoV-2-Arjunglucoside-I (c) SARS-CoV-2-Carnosol (d) SARS-CoV-2-Rosmanol complexes. The hydrogen bond interactions are represented by dashed lines. The amino acid residues involved in the hydrophobic interactions are shown as starbursts.

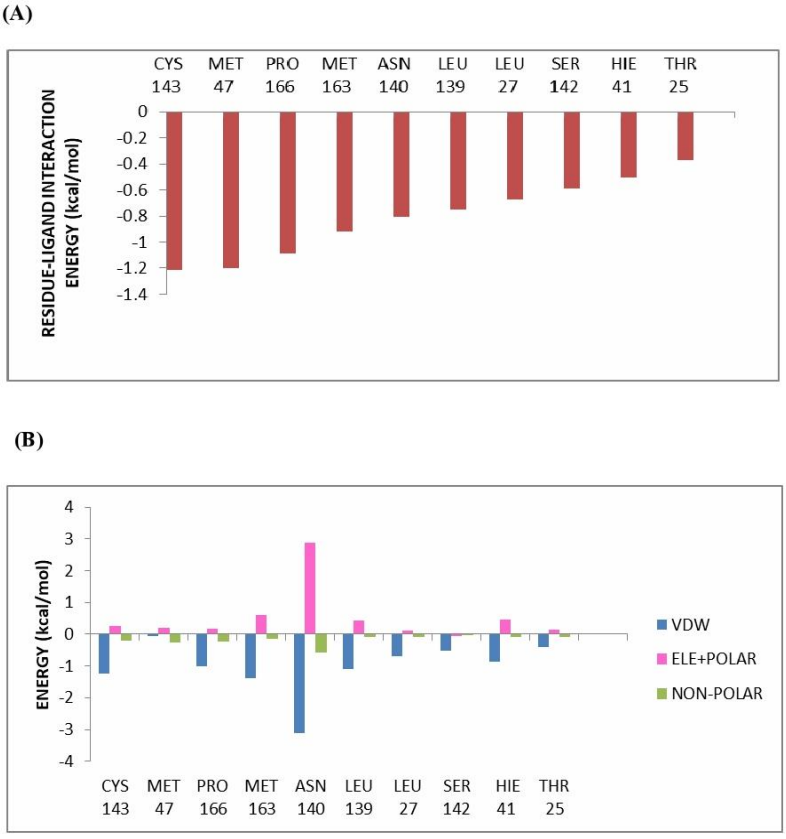

Figure S12. Decomposition of the binding free energy on (A) per-residue basis (B) per-residue basis into the contribution from vdW energy, the sum of electrostatic energy and polar solvation energy, and non-polar solvation energy for SARS-CoV-2 Mpro-Alpha ketoamide complex.

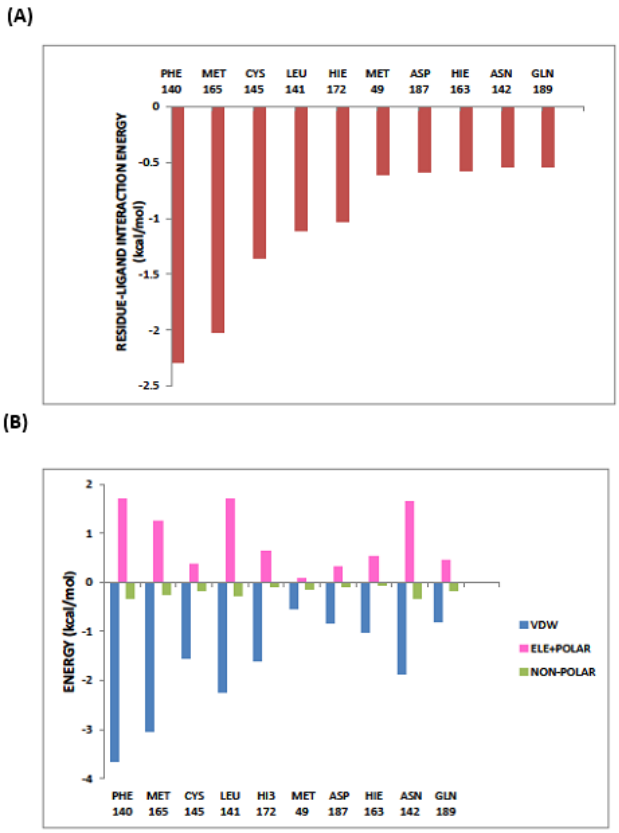

Figure S13. Decomposition of the binding free energy on (A) per-residue basis (B) per-residue basis into the contribution from vdW energy, the sum of electrostatic energy and polar solvation energy, and non-polar solvation energy for SARS-CoV-2 Mpro-Arjunglucoside –I complex

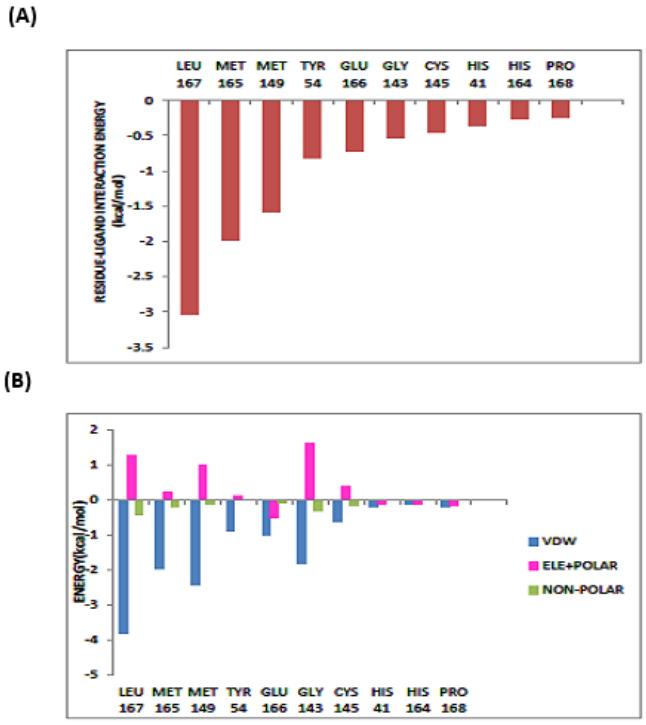

Figure S14. Decomposition of the binding free energy on (A) per-residue basis (B) per-residue basis into the contribution from vdW energy, the sum of electrostatic energy and polar solvation energy, and non-polar solvation energy for SARS-CoV-2 Mpro-Carnosol complex

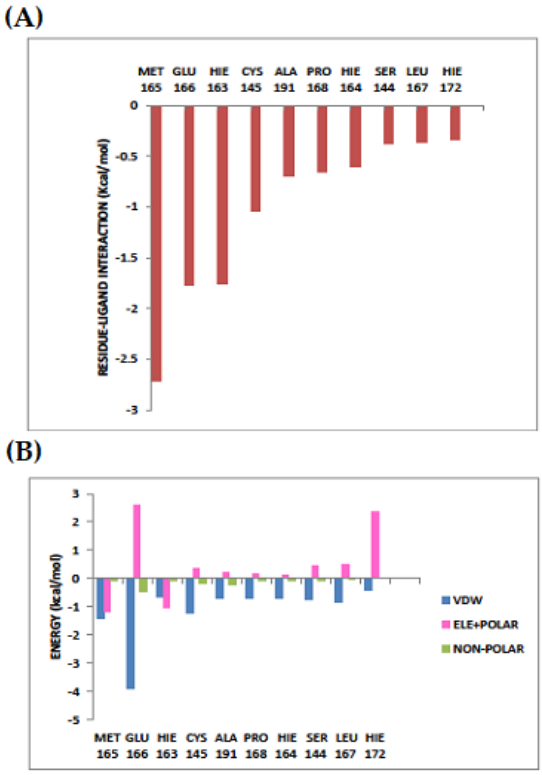

Figure S15. Decomposition of the binding free energy on (A) per-residue basis (B) per-residue basis into the contribution from vdW energy, the sum of electrostatic energy and polar solvation energy, and non-polar solvation energy for SARS-CoV-2 Mpro-Rosmanol complex

Table S1. List of atom-atom interactions (Non-bonded contacts) across the protein-ligand interface in SARS-CoV2 Mpro- AKA complex from PDBsum server

SARS-CoV2 Mpro					Non-bonded contacts	AKA				
Sl.no.	Atom no.	Atom name	Res name	Res no.		Atom no.	Atom name	Res name	Res no.	Distance
1	2609	CD	GLU	165	---	1	O26	AKA	1	3.61
2	2611	OE2	GLU	165	---	1	O26	AKA	1	3.21
3	2631	C	LEU	166	---	5	C31	AKA	1	3.73
4	2633	N	PRO	167	---	5	C31	AKA	1	3.76
5	2945	NE2	GLN	188	---	11	O22	AKA	1	3.11
6	2945	NE2	GLN	188	---	16	C20	AKA	1	3.79
7	2266	CG	ASN	141	---	22	O37	AKA	1	3.65
8	2267	OD1	ASN	141	---	22	O37	AKA	1	3.15
9	2945	NE2	GLN	188	---	23	N38	AKA	1	3.74
10	2603	CB	GLU	165	---	27	C47	AKA	1	3.78
11	2603	CB	GLU	165	---	29	N49	AKA	1	3.43
12	2609	CD	GLU	165	---	29	N49	AKA	1	3.78
13	2610	OE1	GLU	165	---	29	N49	AKA	1	3.37
14	2610	OE1	GLU	165	---	30	C51	AKA	1	3.77
15	2287	OG	SER	143	---	31	C54	AKA	1	3.58
16	2557	CE1	HIE	162	---	31	C54	AKA	1	3.64
17	2559	NE2	HIE	162	---	31	C54	AKA	1	3.58
18	2581	O	HIE	163	---	32	C57	AKA	1	3.85
19	2945	NE2	GLN	188	---	33	O40	AKA	1	3.77
20	787	SD	MET	48	---	37	C13	AKA	1	3.59

SARS-CoV2 Mpro					Non-bonded contacts	AKA				
Sl.no.	Atom no.	Atom name	Res name	Res no.		Atom no.	Atom name	Res name	Res no.	Distance
21	788	CE	MET	48	---	38	C14	AKA	1	3.84
22	788	CE	MET	48	---	39	C28	AKA	1	3.52
23	439	CG2	THR	26	---	40	C26	AKA	1	3.79
24	2267	OD1	ASN	141	---	42	C23	AKA	1	3.24
25	2273	N	GLY	142	---	42	C23	AKA	1	3.87
26	2267	OD1	ASN	141	---	43	C15	AKA	1	3.6

Table S2A. List of atom-atom interactions (Hydrogen bonds) across the protein-protein interface in SARS-Cov2 Mpro- ARJ complex from PDBsum server.

SARS-Cov2 Mpro					Hydrogen bonds	ARJ				
Sl.no.	Atom no.	Atom name	Res name	Res no.		Atom no.	Atom name	Res name	Res no.	Distance
1	795	OG	SER	47	<--	9	O8	ARJG	1	3.24
2	722	NE2	HIE	42	-->	11	O10	ARJG	1	2.98
3	2629	O	HIE	165	<--	11	O10	ARJG	1	3.16

Table S2B. List of atom-atom interactions (Non-bonded contacts)across the protein-protein interface in SARS-Cov2 Mpro- ARJ complex from PDBsum server.

SARS-Cov2 Mpro					Non-bonded contacts	ARJ				
Sl.no	Atom no.	Atom name	Res name	Res no.		Atom no.	Atom name	Res name	Res no.	Distance
1	2272	CB	PHE	141	---	3	O2	ARJG	1	3.13
2	2275	CG	PHE	141	---	3	O2	ARJG	1	3.31
3	2284	CD2	PHE	141	---	3	O2	ARJG	1	3.8
4	2332	CB	SER	145	---	3	O2	ARJG	1	3.54
5	2632	CA	MET	166	---	6	O5	ARJG	1	3.84
6	2645	C	MET	166	---	6	O5	ARJG	1	3.59
7	2647	N	GLU	167	---	6	O5	ARJG	1	3.08
8	2649	CA	GLU	167	---	6	O5	ARJG	1	3.88
9	2651	CB	GLU	167	---	6	O5	ARJG	1	3.46
10	2629	O	HIE	165	---	7	O6	ARJG	1	3.42
11	2632	CA	MET	166	---	7	O6	ARJG	1	3.69
12	792	CB	SER	47	---	9	O8	ARJG	1	3.76
13	795	OG	SER	47	---	9	O8	ARJG	1	3.24
14	836	SD	MET	50	---	9	O8	ARJG	1	3.59
15	830	CB	MET	50	---	10	O9	ARJG	1	3.69
16	836	SD	MET	50	---	10	O9	ARJG	1	3.59
17	837	CE	MET	50	---	10	O9	ARJG	1	3.54
18	2959	CA	ARG	189	---	10	O9	ARJG	1	3.62
19	2979	C	ARG	189	---	10	O9	ARJG	1	3.6
20	2981	N	GLN	190	---	10	O9	ARJG	1	3.55
21	720	CE1	HIE	42	---	11	O10	ARJG	1	3.46
22	722	NE2	HIE	42	---	11	O10	ARJG	1	2.98
23	2629	O	HIE	165	---	11	O10	ARJG	1	3.16

SARS-Cov2 Mpro					Non-bonded contacts	ARJ				
Sl.no	Atom no.	Atom name	Res name	Res no.		Atom no.	Atom name	Res name	Res no.	Distance
24	2634	CB	MET	166	---	11	O10	ARJG	1	3.58
25	2947	CA	ASP	188	---	11	O10	ARJG	1	3.8
26	2955	C	ASP	188	---	11	O10	ARJG	1	3.43
27	2956	O	ASP	188	---	11	O10	ARJG	1	3.45
28	2659	OE2	GLU	167	---	22	C10	ARJG	1	3.45
29	2659	OE2	GLU	167	---	29	C17	ARJG	1	3.58
30	2658	OE1	GLU	167	---	31	C19	ARJG	1	3.68
31	2305	C	LEU	142	---	32	C20	ARJG	1	3.57
32	2306	O	LEU	142	---	32	C20	ARJG	1	3.35
33	2307	N	ASN	143	---	32	C20	ARJG	1	3.73
34	2309	CA	ASN	143	---	32	C20	ARJG	1	3.76
35	2628	C	HIE	165	---	34	C22	ARJG	1	3.58
36	2629	O	HIE	165	---	34	C22	ARJG	1	3.47
37	2630	N	MET	166	---	34	C22	ARJG	1	3.57
38	2632	CA	MET	166	---	34	C22	ARJG	1	3.8
39	2339	N	CYS	146	---	38	C26	ARJG	1	3.78
40	2341	CA	CYS	146	---	38	C26	ARJG	1	3.49
41	2343	CB	CYS	146	---	38	C26	ARJG	1	3.77
42	2346	SG	CYS	146	---	38	C26	ARJG	1	3.78
43	2612	O	HIE	164	---	38	C26	ARJG	1	3.85
44	2630	N	MET	166	---	40	C28	ARJG	1	3.71
45	2645	C	MET	166	---	40	C28	ARJG	1	3.9
46	2646	O	MET	166	---	40	C28	ARJG	1	3.38
47	2745	CD2	HIE	173	---	40	C28	ARJG	1	3.9
48	2337	C	SER	145	---	41	C29	ARJG	1	3.74
49	2338	O	SER	145	---	41	C29	ARJG	1	3.38
50	2634	CB	MET	166	---	47	C35	ARJG	1	3.73
51	2955	C	ASP	188	---	47	C35	ARJG	1	3.7
52	2957	N	ARG	189	---	47	C35	ARJG	1	3.73
53	2980	O	ARG	189	---	47	C35	ARJG	1	3.61

Table S3A. List of atom-atom interactions (Hydrogen bonds)across the protein-protein interface in SARS-Cov2 Mpro- CAN complex from PDBsum server.

SARS-Cov2 Mpro					Hydrogen bonds	CAN				
Sl.no.	Atom no.	Atom name	Res name	Res no.		Atom no.	Atom name	Res name	Res no.	Distance
1	667	NE2	HIE	42	-->	3	O3	CAN	1	3.27

Table S3B. List of atom-atom interactions (Non-bonded contacts) across the protein-protein interface in SARS-Cov2 Mpro- CAN complex from PDBsum server.

SARS-Cov2 Mpro					Non-bonded contacts	CAN				
Sl.no.	Atom no.	Atom name	Res name	Res no.		Atom no.	Atom name	Res name	Res no.	Distance
1	2593	N	GLU	167	---	1	O1	CAN	1	3.28
2	2607	O	GLU	167	---	1	O1	CAN	1	3.5
3	2597	CB	GLU	167	---	1	O1	CAN	1	3.83
4	667	NE2	HIE	42	---	3	O3	CAN	1	3.27
5	669	CD2	HIE	42	---	3	O3	CAN	1	3.76
6	2580	CB	MET	166	---	3	O3	CAN	1	3.8
7	2926	O	ARG	189	---	3	O3	CAN	1	3.78
8	663	CG	HIE	42	---	4	O4	CAN	1	3.72
9	664	ND1	HIE	42	---	4	O4	CAN	1	3.42
10	665	CE1	HIE	42	---	4	O4	CAN	1	2.39
11	667	NE2	HIE	42	---	4	O4	CAN	1	2.1
12	669	CD2	HIE	42	---	4	O4	CAN	1	3.09
13	2563	CB	HIE	165	---	4	O4	CAN	1	3.67
14	2574	C	HIE	165	---	4	O4	CAN	1	3.53
15	2575	O	HIE	165	---	4	O4	CAN	1	2.99
16	2578	CA	MET	166	---	5	C1	CAN	1	3.79
17	2591	C	MET	166	---	5	C1	CAN	1	3.88
18	2580	CB	MET	166	---	5	C1	CAN	1	3.15
19	2587	CE	MET	166	---	5	C1	CAN	1	3.2
20	2593	N	GLU	167	---	5	C1	CAN	1	3.4
21	2606	C	GLU	167	---	5	C1	CAN	1	3.59
22	2607	O	GLU	167	---	5	C1	CAN	1	2.79
23	2580	CB	MET	166	---	6	C2	CAN	1	3.51
24	2587	CE	MET	166	---	7	C3	CAN	1	3.24
25	2606	C	GLU	167	---	7	C3	CAN	1	3.88
26	2607	O	GLU	167	---	7	C3	CAN	1	2.85
27	2972	CB	GLN	193	---	7	C3	CAN	1	3.53
28	2980	NE2	GLN	193	---	7	C3	CAN	1	3.7
29	2578	CA	MET	166	---	8	C4	CAN	1	3.24
30	2591	C	MET	166	---	8	C4	CAN	1	2.85
31	2592	O	MET	166	---	8	C4	CAN	1	3.81
32	2580	CB	MET	166	---	8	C4	CAN	1	3.25
33	2587	CE	MET	166	---	8	C4	CAN	1	3.85
34	2593	N	GLU	167	---	8	C4	CAN	1	2
35	2595	CA	GLU	167	---	8	C4	CAN	1	2.55
36	2606	C	GLU	167	---	8	C4	CAN	1	2.36
37	2607	O	GLU	167	---	8	C4	CAN	1	1.89
38	2597	CB	GLU	167	---	8	C4	CAN	1	3.39
39	2608	N	LEU	168	---	8	C4	CAN	1	3.61
40	2926	O	ARG	189	---	9	C5	CAN	1	3.32

SARS-Cov2 Mpro					Non-bonded contacts	CAN				
Sl.no.	Atom no.	Atom name	Res name	Res no.		Atom no.	Atom name	Res name	Res no.	Distance
41	2929	CA	GLN	190	---	9	C5	CAN	1	3.7
42	2980	NE2	GLN	193	---	9	C5	CAN	1	3.81
43	2587	CE	MET	166	---	10	C6	CAN	1	3.27
44	2957	O	THR	191	---	10	C6	CAN	1	3.39
45	2972	CB	GLN	193	---	10	C6	CAN	1	2.85
46	2975	CG	GLN	193	---	10	C6	CAN	1	2.87
47	2978	CD	GLN	193	---	10	C6	CAN	1	2.81
48	2980	NE2	GLN	193	---	10	C6	CAN	1	2.28
49	2578	CA	MET	166	---	11	C7	CAN	1	2.85
50	2591	C	MET	166	---	11	C7	CAN	1	2.79
51	2580	CB	MET	166	---	11	C7	CAN	1	3.37
52	2593	N	GLU	167	---	11	C7	CAN	1	1.94
53	2595	CA	GLU	167	---	11	C7	CAN	1	2.92
54	2606	C	GLU	167	---	11	C7	CAN	1	3.38
55	2607	O	GLU	167	---	11	C7	CAN	1	3.11
56	2597	CB	GLU	167	---	11	C7	CAN	1	3.19
57	2578	CA	MET	166	---	12	C8	CAN	1	2.93
58	2591	C	MET	166	---	12	C8	CAN	1	3.85
59	2580	CB	MET	166	---	12	C8	CAN	1	2.52
60	2593	N	GLU	167	---	12	C8	CAN	1	3.77
61	2926	O	ARG	189	---	13	C9	CAN	1	2.77
62	2957	O	THR	191	---	13	C9	CAN	1	3.68
63	2975	CG	GLN	193	---	13	C9	CAN	1	3.76
64	2978	CD	GLN	193	---	13	C9	CAN	1	3.32
65	2980	NE2	GLN	193	---	13	C9	CAN	1	2.26
66	2574	C	HIE	165	---	14	C10	CAN	1	3.78
67	2575	O	HIE	165	---	14	C10	CAN	1	3.45
68	2576	N	MET	166	---	14	C10	CAN	1	3.33
69	2578	CA	MET	166	---	14	C10	CAN	1	2.05
70	2591	C	MET	166	---	14	C10	CAN	1	2.82
71	2580	CB	MET	166	---	14	C10	CAN	1	2.44
72	2593	N	GLU	167	---	14	C10	CAN	1	2.68
73	2607	O	GLU	167	---	16	C12	CAN	1	2.89
74	2587	CE	MET	166	---	17	C13	CAN	1	2.6
75	2606	C	GLU	167	---	17	C13	CAN	1	3.37
76	2607	O	GLU	167	---	17	C13	CAN	1	2.64
77	2608	N	LEU	168	---	17	C13	CAN	1	3.86
78	2610	CA	LEU	168	---	17	C13	CAN	1	3.72
79	2615	CG	LEU	168	---	17	C13	CAN	1	3.11
80	2621	CD2	LEU	168	---	17	C13	CAN	1	2.55
81	2972	CB	GLN	193	---	17	C13	CAN	1	3.15

SARS-Cov2 Mpro					Non-bonded contacts	CAN				
Sl.no.	Atom no.	Atom name	Res name	Res no.		Atom no.	Atom name	Res name	Res no.	Distance
82	667	NE2	HIE	42	---	18	C14	CAN	1	3.8
83	2575	O	HIE	165	---	18	C14	CAN	1	3.7
84	2578	CA	MET	166	---	18	C14	CAN	1	3.51
85	2580	CB	MET	166	---	18	C14	CAN	1	2.92
86	2574	C	HIE	165	---	19	C15	CAN	1	2.67
87	2575	O	HIE	165	---	19	C15	CAN	1	2.16
88	2576	N	MET	166	---	19	C15	CAN	1	2.56
89	2578	CA	MET	166	---	19	C15	CAN	1	1.89
90	2591	C	MET	166	---	19	C15	CAN	1	2.96
91	2580	CB	MET	166	---	19	C15	CAN	1	2.78
92	2593	N	GLU	167	---	19	C15	CAN	1	3.23
93	2561	CA	HIE	165	---	20	C16	CAN	1	3.39
94	2574	C	HIE	165	---	20	C16	CAN	1	2.17
95	2575	O	HIE	165	---	20	C16	CAN	1	1.3
96	2576	N	MET	166	---	20	C16	CAN	1	2.74
97	2578	CA	MET	166	---	20	C16	CAN	1	2.67
98	2580	CB	MET	166	---	20	C16	CAN	1	3.14
99	665	CE1	HIE	42	---	21	C17	CAN	1	3.76
100	667	NE2	HIE	42	---	21	C17	CAN	1	3.32
101	2574	C	HIE	165	---	21	C17	CAN	1	3.13
102	2575	O	HIE	165	---	21	C17	CAN	1	2.51
103	2576	N	MET	166	---	21	C17	CAN	1	3.62
104	2578	CA	MET	166	---	21	C17	CAN	1	3.33
105	2580	CB	MET	166	---	21	C17	CAN	1	3.11
106	2287	CA	CYS	146	---	22	C18	CAN	1	3.73
107	2289	CB	CYS	146	---	22	C18	CAN	1	3.27
108	2292	SG	CYS	146	---	22	C18	CAN	1	2.86
109	2559	N	HIE	165	---	22	C18	CAN	1	3.73
110	2561	CA	HIE	165	---	22	C18	CAN	1	2.53
111	2563	CB	HIE	165	---	22	C18	CAN	1	3.5
112	2574	C	HIE	165	---	22	C18	CAN	1	1.69
113	2575	O	HIE	165	---	22	C18	CAN	1	0.55
114	2576	N	MET	166	---	22	C18	CAN	1	2.83
115	2578	CA	MET	166	---	22	C18	CAN	1	3.46
116	2287	CA	CYS	146	---	23	C19	CAN	1	3.8
117	2292	SG	CYS	146	---	23	C19	CAN	1	3.56
118	2550	ND1	HIE	164	---	23	C19	CAN	1	3.11
119	2551	CE1	HIE	164	---	23	C19	CAN	1	3.5
120	2557	C	HIE	164	---	23	C19	CAN	1	3.31
121	2558	O	HIE	164	---	23	C19	CAN	1	3.64
122	2559	N	HIE	165	---	23	C19	CAN	1	2.32

SARS-Cov2 Mpro					Non-bonded contacts	CAN				
Sl.no.	Atom no.	Atom name	Res name	Res no.		Atom no.	Atom name	Res name	Res no.	Distance
123	2561	CA	HIE	165	---	23	C19	CAN	1	1.44
124	2563	CB	HIE	165	---	23	C19	CAN	1	2.82
125	2574	C	HIE	165	---	23	C19	CAN	1	0.8
126	2575	O	HIE	165	---	23	C19	CAN	1	1.3
127	2576	N	MET	166	---	23	C19	CAN	1	1.93
128	2578	CA	MET	166	---	23	C19	CAN	1	3.14
129	2285	N	CYS	146	---	24	C20	CAN	1	3.46
130	2287	CA	CYS	146	---	24	C20	CAN	1	2.91
131	2289	CB	CYS	146	---	24	C20	CAN	1	2.31
132	2292	SG	CYS	146	---	24	C20	CAN	1	2.8
133	2561	CA	HIE	165	---	24	C20	CAN	1	3.74
134	2574	C	HIE	165	---	24	C20	CAN	1	2.96
135	2575	O	HIE	165	---	24	C20	CAN	1	1.92
136	2576	N	MET	166	---	24	C20	CAN	1	3.89

Table S4A. List of atom-atom interactions (Hydrogen bonds) across the protein-protein interface in SARS-Cov2 Mpro- ROS complex from PDBsum server.

SARS-Cov2 Mpro					Hydrogen bonds	ROS				
Sl.no.	Atom no.	Atom name	Res name	Res no.		Atom no.	Atom name	Res name	Res no.	Distance
1	2234	O	PHE	141	<--	1	O1	ROS	1	3.3
2	2554	NE2	HIE	164	-->	3	O3	ROS	1	3.2
3	2608	O	GLU	167	<--	5	O5	ROS	1	3.28

Table S4B. List of atom-atom interactions (Non-bonded contacts) across the protein-protein interface in SARS-Cov2 Mpro- ROS complex from PDBsum server.

SARS-Cov2 Mpro					Non-bonded contacts	ROS				
Sl.no.	Atom no.	Atom name	Res name	Res no.		Atom no.	Atom name	Res name	Res no.	Distance
1	2234	O	PHE	141	---	1	O1	ROS	1	3.3
2	2598	CB	GLU	167	---	1	O1	ROS	1	3.81
3	2605	OE1	GLU	167	---	1	O1	ROS	1	3.9
4	2552	CE1	HIE	164	---	3	O3	ROS	1	3.82
5	2554	NE2	HIE	164	---	3	O3	ROS	1	3.2
6	2579	CA	MET	166	---	3	O3	ROS	1	3.38
7	2592	C	MET	166	---	3	O3	ROS	1	3.15
8	2593	O	MET	166	---	3	O3	ROS	1	3.75
9	2594	N	GLU	167	---	3	O3	ROS	1	3.14
10	2598	CB	GLU	167	---	3	O3	ROS	1	3.55
11	2579	CA	MET	166	---	4	O4	ROS	1	3.88
12	2581	CB	MET	166	---	4	O4	ROS	1	3.52
13	2594	N	GLU	167	---	4	O4	ROS	1	3.47
14	2944	O	GLN	190	---	4	O4	ROS	1	3.51
15	2608	O	GLU	167	---	5	O5	ROS	1	3.28
16	2944	O	GLN	190	---	5	O5	ROS	1	3.75

SARS-Cov2 Mpro					Non-bonded contacts	ROS				
Sl.no.	Atom no.	Atom name	Res name	Res no.		Atom no.	Atom name	Res name	Res no.	Distance
17	2234	O	PHE	141	---	9	C4	ROS	1	3.46
18	2594	N	GLU	167	---	12	C7	ROS	1	3.85
19	2598	CB	GLU	167	---	12	C7	ROS	1	3.68
20	2604	CD	GLU	167	---	14	C9	ROS	1	3.83
21	2605	OE1	GLU	167	---	14	C9	ROS	1	3.88
22	2606	OE2	GLU	167	---	14	C9	ROS	1	3.74
23	2594	N	GLU	167	---	15	C10	ROS	1	3.69
24	2598	CB	GLU	167	---	15	C10	ROS	1	3.56
25	2598	CB	GLU	167	---	16	C11	ROS	1	3.7
26	2234	O	PHE	141	---	17	C12	ROS	1	3.74
27	2252	C	LEU	142	---	17	C12	ROS	1	3.89
28	2253	O	LEU	142	---	17	C12	ROS	1	3.12
29	2282	OG	SER	145	---	17	C12	ROS	1	3.21
30	2594	N	GLU	167	---	19	C14	ROS	1	3.58
31	2608	O	GLU	167	---	19	C14	ROS	1	3.84
32	2598	CB	GLU	167	---	20	C15	ROS	1	3.85
33	2604	CD	GLU	167	---	20	C15	ROS	1	3.88
34	2606	OE2	GLU	167	---	20	C15	ROS	1	3.41
35	2608	O	GLU	167	---	22	C17	ROS	1	3.49
36	2608	O	GLU	167	---	24	C19	ROS	1	3.6
37	2626	C	LEU	168	---	24	C19	ROS	1	3.77
38	2963	CB	ALA	192	---	25	C20	ROS	1	3.78

Table S5. Hydrogen bonding contacts between SARS-CoV-2 Mpro and AKA during the course of 50 ns MD simulation

Acceptor	DonorH	Donor	Frames	Frac	AvgDist	AvgAng
CYS_144@HG	AKA_1@H36	AKA_1@N36	445	0.0890	2.7074	154.1059
MET_164@HA	AKA_1@HO40	AKA_1@O40	133	0.0266	2.7883	150.6348
MET_48@HG3	AKA_1@H133	AKA_1@C13	121	0.0242	2.9259	147.4516
GLU_165@H	AKA_1@H423	AKA_1@C42	102	0.0204	2.8931	148.3543
SER_143@HG	AKA_1@H543	AKA_1@C54	92	0.0184	2.9217	148.6688
GLN_188@HE21	AKA_1@H20	AKA_1@C20	91	0.0182	2.8470	154.5173
HIE_162@HE2	AKA_1@H543	AKA_1@C54	85	0.0170	2.8682	144.0108
MET_48@HG3	AKA_1@H132	AKA_1@C13	83	0.0166	2.9333	145.5845
MET_164@HA	AKA_1@H422	AKA_1@C42	78	0.0156	2.9295	143.5477
MET_164@HB2	AKA_1@HO40	AKA_1@O40	71	0.0142	2.8466	147.8645
MET_164@HB3	AKA_1@HO40	AKA_1@O40	69	0.0138	2.8420	148.7274
CYS_144@HG	AKA_1@H57	AKA_1@C57	55	0.0110	2.8848	150.4686
SER_143@HG	AKA_1@H512	AKA_1@C51	51	0.0102	2.9042	141.9291
MET_164@HA	AKA_1@H423	AKA_1@C42	49	0.0098	2.9206	139.9120
GLY_142@H	AKA_1@H26	AKA_1@C26	39	0.0078	2.8940	152.3115
GLU_165@OE2	AKA_1@H49	AKA_1@N49	39	0.0078	2.9236	147.4092
GLN_188@HE21	AKA_1@H302	AKA_1@C30	39	0.0078	2.8069	147.5447
HIE_171@HE2	AKA_1@H513	AKA_1@C51	36	0.0072	2.9235	159.0629
GLU_165@HB2	AKA_1@H49	AKA_1@N49	35	0.0070	2.6979	143.5345
GLU_165@H	AKA_1@HO40	AKA_1@O40	30	0.0060	2.8164	152.2591
GLN_188@HE21	AKA_1@HO40	AKA_1@O40	29	0.0058	2.6336	150.3850
LEU_28@HB3	AKA_1@H23	AKA_1@C23	28	0.0056	2.9511	145.3795
GLU_165@H	AKA_1@H422	AKA_1@C42	28	0.0056	2.8748	143.2061
ASN_141@HB2	AKA_1@H16	AKA_1@C16	26	0.0052	2.9343	142.3358
HIE_162@HE2	AKA_1@H513	AKA_1@C51	25	0.0050	2.8062	144.7324
ASN_141@HA	AKA_1@H45	AKA_1@C45	24	0.0048	2.9383	142.8056
LEU_28@HD23	AKA_1@H23	AKA_1@C23	23	0.0046	2.9319	140.4834
GLN_188@HE22	AKA_1@H20	AKA_1@C20	23	0.0046	2.8656	150.5083
MET_164@HA	AKA_1@H57	AKA_1@C57	21	0.0042	2.9307	141.0176
HIE_162@HE2	AKA_1@H542	AKA_1@C54	20	0.0040	2.8347	144.4822
PRO_167@HA	AKA_1@H323	AKA_1@C32	20	0.0040	2.9511	142.4544
GLN_188@HE22	AKA_1@HO40	AKA_1@O40	20	0.0040	2.8150	152.4242
ASN_141@HA	AKA_1@H543	AKA_1@C54	18	0.0036	2.9383	141.2797

CYS_144@HG	AKA_1@H15	AKA_1@C15	18	0.0036	2.7967	144.5274
PRO_167@HA	AKA_1@H321	AKA_1@C32	18	0.0036	2.9570	145.3398
PRO_167@HA	AKA_1@H312	AKA_1@C31	17	0.0034	2.9369	141.3913
GLN_188@HE21	AKA_1@H29	AKA_1@C29	17	0.0034	2.9033	151.8247
MET_48@HG3	AKA_1@H28	AKA_1@C28	16	0.0032	2.9194	144.6405
GLY_142@HA2	AKA_1@H26	AKA_1@C26	16	0.0032	2.9230	143.9647
PRO_167@HA	AKA_1@H322	AKA_1@C32	16	0.0032	2.9260	143.1036
GLU_165@HB2	AKA_1@H513	AKA_1@C51	15	0.0030	2.9410	140.2304
GLU_165@HB3	AKA_1@H49	AKA_1@N49	14	0.0028	2.8456	140.1403
HIE_42@HB3	AKA_1@H15	AKA_1@C15	12	0.0024	2.9506	141.1502
PRO_167@HA	AKA_1@H311	AKA_1@C31	12	0.0024	2.9596	142.6630
HIE_162@HE2	AKA_1@H512	AKA_1@C51	11	0.0022	2.8047	143.0221
HIE_162@HE2	AKA_1@H49	AKA_1@N49	11	0.0022	2.7282	148.3561
GLN_188@HG3	AKA_1@HO40	AKA_1@O40	10	0.0020	2.8142	143.5628
HIE_42@HB2	AKA_1@H23	AKA_1@C23	9	0.0018	2.9299	144.6990
MET_48@HE2	AKA_1@H133	AKA_1@C13	9	0.0018	2.9203	143.2736
PHE_139@HB3	AKA_1@H512	AKA_1@C51	9	0.0018	2.9374	137.6838
ASN_141@HD21	AKA_1@H223	AKA_1@C22	9	0.0018	2.8956	148.7954
HIE_162@HE1	AKA_1@H542	AKA_1@C54	9	0.0018	2.9424	140.7393
GLN_188@HE21	AKA_1@H222	AKA_1@C22	9	0.0018	2.8798	144.4997
MET_48@HE1	AKA_1@H133	AKA_1@C13	8	0.0016	2.9150	138.6394
MET_164@HA	AKA_1@H542	AKA_1@C54	8	0.0016	2.9417	140.2736
GLN_188@HE21	AKA_1@H343	AKA_1@C34	8	0.0016	2.9056	146.6975
LEU_28@HD21	AKA_1@H23	AKA_1@C23	7	0.0014	2.9234	139.2521
LEU_28@HD22	AKA_1@H23	AKA_1@C23	7	0.0014	2.9376	141.6258
LEU_28@HD23	AKA_1@H15	AKA_1@C15	7	0.0014	2.9369	144.7682
PHE_139@HB3	AKA_1@H49	AKA_1@N49	7	0.0014	2.8158	143.3579
ASN_141@HB2	AKA_1@H17	AKA_1@C17	7	0.0014	2.9735	141.0133
ASN_141@HD21	AKA_1@H302	AKA_1@C30	7	0.0014	2.8699	150.2013
HIE_171@HE2	AKA_1@H49	AKA_1@N49	7	0.0014	2.8803	148.9560
LEU_28@HB3	AKA_1@H25	AKA_1@C25	6	0.0012	2.9632	141.5695
MET_48@HE1	AKA_1@H132	AKA_1@C13	6	0.0012	2.9190	140.5805
PHE_139@HB2	AKA_1@H513	AKA_1@C51	6	0.0012	2.9272	139.7714
HIE_162@HE1	AKA_1@H513	AKA_1@C51	6	0.0012	2.9459	141.8817
PRO_167@HG3	AKA_1@H321	AKA_1@C32	6	0.0012	2.9580	140.1403
PRO_167@HA	AKA_1@H313	AKA_1@C31	6	0.0012	2.9720	144.8805
GLN_188@HE21	AKA_1@H38	AKA_1@N38	6	0.0012	2.8718	143.3934
LEU_28@HD21	AKA_1@H15	AKA_1@C15	5	0.0010	2.9715	143.0574
MET_48@HG3	AKA_1@H15	AKA_1@C15	5	0.0010	2.9596	138.8872
MET_48@HE2	AKA_1@H132	AKA_1@C13	5	0.0010	2.9290	143.2715
ASN_141@HD22	AKA_1@H16	AKA_1@C16	5	0.0010	2.9228	159.0690
CYS_144@HB2	AKA_1@H23	AKA_1@C23	5	0.0010	2.9312	142.3192
THR_27@H	AKA_1@H25	AKA_1@C25	4	0.0008	2.8721	145.8010
HIE_42@HB3	AKA_1@H132	AKA_1@C13	4	0.0008	2.9422	143.3516
HIE_42@HD2	AKA_1@H132	AKA_1@C13	4	0.0008	2.8735	143.5491
MET_48@HG3	AKA_1@H342	AKA_1@C34	4	0.0008	2.8955	139.2332
MET_48@HE3	AKA_1@H132	AKA_1@C13	4	0.0008	2.9245	148.7314
GLY_142@HA2	AKA_1@H23	AKA_1@C23	4	0.0008	2.9193	144.4991
CYS_144@HB2	AKA_1@H15	AKA_1@C15	4	0.0008	2.9643	145.8708
LEU_28@HG	AKA_1@H25	AKA_1@C25	3	0.0006	2.9407	139.4884
MET_48@HE3	AKA_1@H15	AKA_1@C15	3	0.0006	2.9562	141.2947
LEU_140@HA	AKA_1@H512	AKA_1@C51	3	0.0006	2.9354	146.7222
ASN_141@HD21	AKA_1@H222	AKA_1@C22	3	0.0006	2.8865	165.9303
GLU_165@HB3	AKA_1@H312	AKA_1@C31	3	0.0006	2.9147	142.2889
GLU_165@HG2	AKA_1@H312	AKA_1@C31	3	0.0006	2.9643	141.8007
PRO_167@HA	AKA_1@H332	AKA_1@C33	3	0.0006	2.9639	148.1285
GLN_188@HG2	AKA_1@HO40	AKA_1@O40	3	0.0006	2.9357	142.1318
GLN_188@NE2	AKA_1@HO40	AKA_1@O40	3	0.0006	2.9906	142.5123
GLN_188@HE21	AKA_1@H331	AKA_1@C33	3	0.0006	2.8760	153.2808
THR_26@HG21	AKA_1@H23	AKA_1@C23	2	0.0004	2.9406	136.1919
THR_26@HG22	AKA_1@H26	AKA_1@C26	2	0.0004	2.8999	139.3346
THR_26@HG23	AKA_1@H26	AKA_1@C26	2	0.0004	2.9872	139.6087
THR_26@HG23	AKA_1@H23	AKA_1@C23	2	0.0004	2.9411	153.3890
LEU_28@HB3	AKA_1@H26	AKA_1@C26	2	0.0004	2.9625	142.7899
LEU_28@HD21	AKA_1@H28	AKA_1@C28	2	0.0004	2.9481	138.9796
HIE_42@HB2	AKA_1@H132	AKA_1@C13	2	0.0004	2.9514	138.5320
HIE_42@HB2	AKA_1@H15	AKA_1@C15	2	0.0004	2.9652	143.3415
MET_48@HB2	AKA_1@H342	AKA_1@C34	2	0.0004	2.9202	141.5330
MET_48@HE1	AKA_1@H15	AKA_1@C15	2	0.0004	2.9404	142.3951
PHE_139@HB2	AKA_1@H512	AKA_1@C51	2	0.0004	2.9053	137.4628
PHE_139@HB2	AKA_1@H49	AKA_1@N49	2	0.0004	2.8657	151.7647
LEU_140@HA	AKA_1@H49	AKA_1@N49	2	0.0004	2.6743	145.4708
ASN_141@HD22	AKA_1@H343	AKA_1@C34	2	0.0004	2.9464	140.4500
GLY_142@H	AKA_1@H23	AKA_1@C23	2	0.0004	2.9016	156.3507
CYS_144@HG	AKA_1@H422	AKA_1@C42	2	0.0004	2.8550	144.8617

GLU_165@HB2	AKA_1@H542	AKA_1@C54	2	0.0004	2.8957	136.9232
GLU_165@OE1	AKA_1@H49	AKA_1@N49	2	0.0004	2.9401	152.5071
PRO_167@HG3	AKA_1@H323	AKA_1@C32	2	0.0004	2.9655	143.2397
PRO_167@HG3	AKA_1@H322	AKA_1@C32	2	0.0004	2.9603	135.7135
GLN_188@OE1	AKA_1@HO40	AKA_1@O40	2	0.0004	2.8977	149.8754
GLN_188@HE21	AKA_1@H223	AKA_1@C22	2	0.0004	2.8963	145.3123
THR_26@HG21	AKA_1@H26	AKA_1@C26	1	0.0002	2.9768	143.9186
THR_26@HG22	AKA_1@H23	AKA_1@C23	1	0.0002	2.9931	136.8754
THR_26@HG22	AKA_1@H25	AKA_1@C25	1	0.0002	2.9950	136.1832
THR_27@H	AKA_1@H26	AKA_1@C26	1	0.0002	2.9361	135.1606
HIE_42@HB3	AKA_1@H23	AKA_1@C23	1	0.0002	2.9187	135.0847
HIE_42@HB3	AKA_1@H28	AKA_1@C28	1	0.0002	2.9981	140.4374
MET_48@HB3	AKA_1@H133	AKA_1@C13	1	0.0002	2.9491	139.9618
MET_48@HG2	AKA_1@H132	AKA_1@C13	1	0.0002	2.9361	150.6235
MET_48@HE2	AKA_1@H28	AKA_1@C28	1	0.0002	2.8652	144.5446
MET_48@HE2	AKA_1@H15	AKA_1@C15	1	0.0002	2.9789	156.1584
MET_48@HE3	AKA_1@H133	AKA_1@C13	1	0.0002	2.8988	146.9910
PHE_139@O	AKA_1@H49	AKA_1@N49	1	0.0002	2.9879	136.3334
ASN_141@H	AKA_1@H17	AKA_1@C17	1	0.0002	2.9517	138.7430
ASN_141@HA	AKA_1@H512	AKA_1@C51	1	0.0002	2.9557	162.9039
ASN_141@HD21	AKA_1@H16	AKA_1@C16	1	0.0002	2.8486	146.4685
ASN_141@HD22	AKA_1@H223	AKA_1@C22	1	0.0002	2.7809	169.8947
GLY_142@HA2	AKA_1@H25	AKA_1@C25	1	0.0002	2.9706	135.1673
CYS_144@HG	AKA_1@H542	AKA_1@C54	1	0.0002	2.7988	135.0914
HIE_162@NE2	AKA_1@H49	AKA_1@N49	1	0.0002	2.8839	142.5825
MET_164@HA	AKA_1@H513	AKA_1@C51	1	0.0002	2.9643	137.0719
MET_164@HB3	AKA_1@H57	AKA_1@C57	1	0.0002	2.9771	141.9609
MET_164@HE2	AKA_1@HO40	AKA_1@O40	1	0.0002	2.9263	139.6361
GLU_165@CB	AKA_1@H49	AKA_1@N49	1	0.0002	2.9897	143.6415
GLU_165@HB3	AKA_1@H313	AKA_1@C31	1	0.0002	2.9204	136.8891
GLU_165@CD	AKA_1@H49	AKA_1@N49	1	0.0002	2.9699	152.3993
PRO_167@HD3	AKA_1@H321	AKA_1@C32	1	0.0002	2.9049	141.2130
PRO_167@HD3	AKA_1@H313	AKA_1@C31	1	0.0002	2.9984	140.2657
PRO_167@HD3	AKA_1@H311	AKA_1@C31	1	0.0002	2.9383	139.1181
PRO_167@HG3	AKA_1@H312	AKA_1@C31	1	0.0002	2.8790	136.0450
PRO_167@HA	AKA_1@H333	AKA_1@C33	1	0.0002	2.9860	150.9236
PRO_167@HA	AKA_1@H331	AKA_1@C33	1	0.0002	2.9922	138.3995
HIE_171@HD2	AKA_1@H513	AKA_1@C51	1	0.0002	2.9246	143.4495
GLN_188@HB2	AKA_1@HO40	AKA_1@O40	1	0.0002	2.9930	144.8024
GLN_188@HG3	AKA_1@H343	AKA_1@C34	1	0.0002	2.9349	135.1555
GLN_188@HE21	AKA_1@H342	AKA_1@C34	1	0.0002	2.9160	136.6418
GLN_188@HE22	AKA_1@H132	AKA_1@C13	1	0.0002	2.9362	142.7907
GLN_188@HE22	AKA_1@H38	AKA_1@N38	1	0.0002	2.5080	143.3314
GLN_188@HE22	AKA_1@H303	AKA_1@C30	1	0.0002	2.9861	143.5289
GLN_188@HE22	AKA_1@H302	AKA_1@C30	1	0.0002	2.9852	141.3197
GLN_188@HE22	AKA_1@H331	AKA_1@C33	1	0.0002	2.9604	136.3564

Table S6. Hydrogen bonding contacts between SARS-CoV-2 Mpro and ARJ during the course of 50 ns MD simulation.

Acceptor	DonorH	Donor	Frames	Frac	AvgDist	AvgAng
ASP_188@HA	ARJ_1@HO7	ARJ_1@O10	571	0.1142	2.6643	150.7860
PHE_141@HB3	ARJ_1@HO2	ARJ_1@O2	461	0.0922	2.7630	148.7595
ASP_188@HB2	ARJ_1@HO7	ARJ_1@O10	347	0.0694	2.8161	152.4070
HIE_42@HE2	ARJ_1@HO7	ARJ_1@O10	271	0.0542	2.7380	151.2685
PHE_141@HB2	ARJ_1@HO2	ARJ_1@O2	259	0.0518	2.7962	148.2960
GLN_190@HG2	ARJ_1@HO6	ARJ_1@O9	249	0.0498	2.7900	151.7154
MET_166@HB3	ARJ_1@HO7	ARJ_1@O10	238	0.0476	2.6909	148.4856
GLU_167@H	ARJ_1@HC43	ARJ_1@C30	228	0.0456	2.8754	147.1513
MET_166@HA	ARJ_1@HC28	ARJ_1@C22	225	0.0450	2.9482	142.5734
HIE_173@HE2	ARJ_1@HC19	ARJ_1@C17	195	0.0390	2.8986	153.7576
ASN_143@HA	ARJ_1@HC25	ARJ_1@C20	127	0.0254	2.9369	141.5536
SER_145@HB2	ARJ_1@HO2	ARJ_1@O2	127	0.0254	2.7266	142.1694
GLN_190@HG2	ARJ_1@HO5	ARJ_1@O8	122	0.0244	2.8106	152.6836
ASN_143@HB2	ARJ_1@HO3	ARJ_1@O3	97	0.0194	2.7799	146.5442
GLN_190@HG3	ARJ_1@HO6	ARJ_1@O9	94	0.0188	2.7862	146.1134
LEU_142@HD23	ARJ_1@HO1	ARJ_1@O1	82	0.0164	2.8221	153.6248
HIE_164@HB3	ARJ_1@HC37	ARJ_1@C28	81	0.0162	2.9530	141.3305
HIE_164@HB3	ARJ_1@HC42	ARJ_1@C29	77	0.0154	2.9572	140.7743
CYS_146@HA	ARJ_1@HC36	ARJ_1@C26	65	0.0130	2.9170	140.9137
MET_50@HB3	ARJ_1@HO6	ARJ_1@O9	62	0.0124	2.7969	146.9796
HIE_164@HB3	ARJ_1@HC39	ARJ_1@C28	56	0.0112	2.9452	141.5622
CYS_146@HG	ARJ_1@HC29	ARJ_1@C22	50	0.0100	2.8192	146.0053
HIE_164@HB3	ARJ_1@HC41	ARJ_1@C29	48	0.0096	2.9518	141.3807

HIE_164@HB3	ARJ_1@HC38	ARJ_1@C28	48	0.0096	2.9423	141.0822
MET_166@HB2	ARJ_1@HO7	ARJ_1@O10	47	0.0094	2.7845	149.7205
LEU_142@HD21	ARJ_1@HO1	ARJ_1@O1	46	0.0092	2.8303	151.5881
LEU_142@HD22	ARJ_1@HO1	ARJ_1@O1	46	0.0092	2.8380	153.5332
GLN_190@HE21	ARJ_1@HO5	ARJ_1@O8	45	0.0090	2.7414	148.0621
MET_50@HE2	ARJ_1@HC49	ARJ_1@C35	37	0.0074	2.9196	143.4547
HIE_42@NE2	ARJ_1@HO7	ARJ_1@O10	36	0.0072	2.9407	150.4417
HIE_165@O	ARJ_1@HO7	ARJ_1@O10	35	0.0070	2.9222	152.8361
MET_166@HB3	ARJ_1@HC48	ARJ_1@C35	32	0.0064	2.9302	144.1147
PHE_141@HB2	ARJ_1@HC27	ARJ_1@C21	29	0.0058	2.9520	140.2926
MET_50@HE3	ARJ_1@HO7	ARJ_1@O10	27	0.0054	2.7905	148.1959
HIE_164@HB3	ARJ_1@HC40	ARJ_1@C29	26	0.0052	2.9513	142.8151
ASP_188@O	ARJ_1@HO7	ARJ_1@O10	25	0.0050	2.8931	146.7014
MET_50@HE1	ARJ_1@HO7	ARJ_1@O10	24	0.0048	2.8122	150.8875
MET_50@HE2	ARJ_1@HO7	ARJ_1@O10	24	0.0048	2.8438	151.5137
MET_50@HE3	ARJ_1@HC49	ARJ_1@C35	23	0.0046	2.9195	140.9035
ARG_189@HA	ARJ_1@HO6	ARJ_1@O9	22	0.0044	2.8763	145.8581
SER_47@HB3	ARJ_1@HO5	ARJ_1@O8	20	0.0040	2.8279	145.6020
MET_50@HE3	ARJ_1@HO6	ARJ_1@O9	20	0.0040	2.7761	145.6489
MET_50@HE1	ARJ_1@HO6	ARJ_1@O9	19	0.0038	2.8038	145.5653
MET_50@HE1	ARJ_1@HC49	ARJ_1@C35	19	0.0038	2.9411	146.2674
MET_50@HE2	ARJ_1@HO6	ARJ_1@O9	19	0.0038	2.7818	150.4437
GLN_190@HA	ARJ_1@HO6	ARJ_1@O9	18	0.0036	2.6847	139.8129
MET_50@HB2	ARJ_1@HO6	ARJ_1@O9	17	0.0034	2.8623	148.1304
CYS_146@HB2	ARJ_1@HC36	ARJ_1@C26	15	0.0030	2.9550	139.0634
MET_166@HB2	ARJ_1@HC48	ARJ_1@C35	15	0.0030	2.9536	146.9037
HIE_42@HE1	ARJ_1@HO7	ARJ_1@O10	14	0.0028	2.9370	152.6865
CYS_146@HG	ARJ_1@HC35	ARJ_1@C26	14	0.0028	2.8360	141.7552
HIE_164@HB2	ARJ_1@HC41	ARJ_1@C29	14	0.0028	2.9504	141.1899
PHE_141@CB	ARJ_1@HO2	ARJ_1@O2	13	0.0026	2.9773	148.4441
GLN_190@NE2	ARJ_1@HO5	ARJ_1@O8	12	0.0024	2.9448	151.2503
MET_50@HE1	ARJ_1@HC47	ARJ_1@C34	11	0.0022	2.9226	140.6461
LEU_142@HD23	ARJ_1@HC18	ARJ_1@C16	10	0.0020	2.9470	145.2834
MET_166@HB2	ARJ_1@HC46	ARJ_1@C33	10	0.0020	2.9451	143.9946
ASN_143@HD22	ARJ_1@HO3	ARJ_1@O3	9	0.0018	2.8410	147.3636
HIE_164@HB2	ARJ_1@HC42	ARJ_1@C29	9	0.0018	2.9759	143.0021
HIE_173@HD2	ARJ_1@HC38	ARJ_1@C28	9	0.0018	2.9387	140.3241
SER_47@HG	ARJ_1@HO5	ARJ_1@O8	8	0.0016	2.8241	142.7650
MET_50@HE2	ARJ_1@HC47	ARJ_1@C34	8	0.0016	2.9359	142.1225
MET_50@HE3	ARJ_1@HC47	ARJ_1@C34	8	0.0016	2.9442	147.2580
CYS_146@HA	ARJ_1@HC35	ARJ_1@C26	8	0.0016	2.9369	136.6239
GLN_190@OE1	ARJ_1@HO6	ARJ_1@O9	8	0.0016	2.9304	154.6183
GLN_190@OE1	ARJ_1@HO5	ARJ_1@O8	8	0.0016	2.8767	159.5965
LEU_142@HD23	ARJ_1@HO3	ARJ_1@O3	7	0.0014	2.8831	151.6738
MET_166@HE1	ARJ_1@HO7	ARJ_1@O10	7	0.0014	2.7483	146.0204
MET_166@HE3	ARJ_1@HO7	ARJ_1@O10	7	0.0014	2.8273	149.5741
HIE_173@HD2	ARJ_1@HC37	ARJ_1@C28	7	0.0014	2.9336	140.6752
GLN_190@HE22	ARJ_1@HO5	ARJ_1@O8	7	0.0014	2.5860	151.9901
LEU_142@HD21	ARJ_1@HC9	ARJ_1@C11	6	0.0012	2.9659	139.2224
LEU_142@HD22	ARJ_1@HC18	ARJ_1@C16	6	0.0012	2.9543	145.2881
LEU_142@HD23	ARJ_1@HC9	ARJ_1@C11	6	0.0012	2.9429	140.4876
HIE_164@HB2	ARJ_1@HC40	ARJ_1@C29	6	0.0012	2.9290	141.9053
GLN_190@HG3	ARJ_1@HO5	ARJ_1@O8	6	0.0012	2.9351	147.7900
HIE_42@HD2	ARJ_1@HO7	ARJ_1@O10	5	0.0010	2.7843	146.2467
MET_50@HB2	ARJ_1@HO5	ARJ_1@O8	5	0.0010	2.8086	138.7386
LEU_142@HD12	ARJ_1@HO3	ARJ_1@O3	5	0.0010	2.8322	150.5287
LEU_142@HD22	ARJ_1@HO3	ARJ_1@O3	5	0.0010	2.8518	143.9985
ASN_143@H	ARJ_1@HO3	ARJ_1@O3	5	0.0010	2.6854	138.2609
SER_145@HB2	ARJ_1@HC41	ARJ_1@C29	5	0.0010	2.9787	147.8573
GLU_167@HB2	ARJ_1@HC19	ARJ_1@C17	5	0.0010	2.9622	138.7334
ASP_188@C	ARJ_1@HO7	ARJ_1@O10	5	0.0010	2.9496	150.4623
ARG_189@H	ARJ_1@HO7	ARJ_1@O10	5	0.0010	2.8487	151.2504
SER_47@HB2	ARJ_1@HO5	ARJ_1@O8	4	0.0008	2.6687	146.4748
PHE_141@HD2	ARJ_1@HC27	ARJ_1@C21	4	0.0008	2.9615	150.7528
LEU_142@HG	ARJ_1@HO1	ARJ_1@O1	4	0.0008	2.6922	143.8127
LEU_142@HD21	ARJ_1@HO3	ARJ_1@O3	4	0.0008	2.7970	148.3502
MET_166@HA	ARJ_1@HC43	ARJ_1@C30	4	0.0008	2.8688	141.2114
MET_166@HE3	ARJ_1@HC48	ARJ_1@C35	4	0.0008	2.9385	143.2884
GLN_190@HE22	ARJ_1@HC45	ARJ_1@C32	4	0.0008	2.7265	146.8765
HIE_42@HE2	ARJ_1@HC48	ARJ_1@C35	3	0.0006	2.8802	141.1964
MET_50@HE3	ARJ_1@HO5	ARJ_1@O8	3	0.0006	2.8604	149.4380
MET_50@HE3	ARJ_1@HC48	ARJ_1@C35	3	0.0006	2.9205	143.7412
LEU_142@HD21	ARJ_1@HC18	ARJ_1@C16	3	0.0006	2.9542	143.1910
ASN_143@HB2	ARJ_1@HC2	ARJ_1@C5	3	0.0006	2.9326	143.1548
SER_145@HB2	ARJ_1@HC42	ARJ_1@C29	3	0.0006	2.9738	143.6541

SER_145@HB3	ARJ_1@HO2	ARJ_1@O2	3	0.0006	2.8757	141.0352
MET_166@HE2	ARJ_1@HO7	ARJ_1@O10	3	0.0006	2.8754	145.2699
MET_166@HE3	ARJ_1@HC46	ARJ_1@C33	3	0.0006	2.9228	140.2570
HIE_173@HD2	ARJ_1@HC39	ARJ_1@C28	3	0.0006	2.9652	140.7052
VAL_187@O	ARJ_1@HO7	ARJ_1@O10	3	0.0006	2.9152	147.2164
SER_47@OG	ARJ_1@HO5	ARJ_1@O8	2	0.0004	2.9246	140.8956
SER_47@HG	ARJ_1@HO4	ARJ_1@O7	2	0.0004	2.8088	160.1580
ASN_143@HD22	ARJ_1@HC2	ARJ_1@C5	2	0.0004	2.8800	140.6784
SER_145@HB2	ARJ_1@HC40	ARJ_1@C29	2	0.0004	2.9447	145.7952
HIE_164@HD2	ARJ_1@HC40	ARJ_1@C29	2	0.0004	2.9639	137.2822
MET_166@H	ARJ_1@HC38	ARJ_1@C28	2	0.0004	2.8780	138.1757
MET_166@HB3	ARJ_1@HC49	ARJ_1@C35	2	0.0004	2.9425	146.4705
MET_166@HE2	ARJ_1@HC48	ARJ_1@C35	2	0.0004	2.9146	139.8792
GLU_167@HB2	ARJ_1@HC6	ARJ_1@C9	2	0.0004	2.9707	147.3262
ASP_188@HA	ARJ_1@HC49	ARJ_1@C35	2	0.0004	2.9752	141.7915
ASP_188@HA	ARJ_1@HC48	ARJ_1@C35	2	0.0004	2.9493	137.0455
ASP_188@HB3	ARJ_1@HO7	ARJ_1@O10	2	0.0004	2.8789	146.1509
GLN_190@HE21	ARJ_1@HO6	ARJ_1@O9	2	0.0004	2.8714	149.0830
HIE_42@CE1	ARJ_1@HO7	ARJ_1@O10	1	0.0002	2.9846	154.0775
HIE_42@HE2	ARJ_1@HC49	ARJ_1@C35	1	0.0002	2.9952	148.0172
HIE_42@CD2	ARJ_1@HO7	ARJ_1@O10	1	0.0002	2.9578	141.7081
HIE_42@HD2	ARJ_1@HC44	ARJ_1@C31	1	0.0002	2.8834	159.7561
SER_47@HA	ARJ_1@HO5	ARJ_1@O8	1	0.0002	2.8788	139.9278
SER_47@CB	ARJ_1@HO5	ARJ_1@O8	1	0.0002	2.9850	146.8183
MET_50@HG3	ARJ_1@HO6	ARJ_1@O9	1	0.0002	2.9607	149.5440
MET_50@HE1	ARJ_1@HO5	ARJ_1@O8	1	0.0002	2.6461	169.5427
PHE_141@HB2	ARJ_1@HC7	ARJ_1@C10	1	0.0002	2.9628	139.7573
PHE_141@HB2	ARJ_1@HC24	ARJ_1@C20	1	0.0002	2.9942	152.8911
LEU_142@HA	ARJ_1@HC24	ARJ_1@C20	1	0.0002	2.9916	142.3468
LEU_142@HA	ARJ_1@HC9	ARJ_1@C11	1	0.0002	2.9917	140.4049
LEU_142@HD11	ARJ_1@HO3	ARJ_1@O3	1	0.0002	2.8753	162.1344
ASN_143@HA	ARJ_1@HC26	ARJ_1@C20	1	0.0002	2.9079	137.7918
ASN_143@HD22	ARJ_1@HC12	ARJ_1@C12	1	0.0002	2.8376	148.4496
ASN_143@HD22	ARJ_1@HC25	ARJ_1@C20	1	0.0002	2.6279	138.9544
GLY_144@H	ARJ_1@HC25	ARJ_1@C20	1	0.0002	2.7755	140.8893
CYS_146@HA	ARJ_1@HC42	ARJ_1@C29	1	0.0002	2.8974	138.4134
CYS_146@HB2	ARJ_1@HC16	ARJ_1@C15	1	0.0002	2.9726	145.3496
CYS_146@HB2	ARJ_1@HC29	ARJ_1@C22	1	0.0002	2.9700	135.6811
HIE_164@HB3	ARJ_1@HC35	ARJ_1@C26	1	0.0002	2.9536	138.5861
HIE_164@HD2	ARJ_1@HC42	ARJ_1@C29	1	0.0002	2.9581	137.4710
HIE_164@HD2	ARJ_1@HC38	ARJ_1@C28	1	0.0002	2.9396	146.5595
HIE_164@HD2	ARJ_1@HC39	ARJ_1@C28	1	0.0002	2.9744	139.8307
MET_166@HB3	ARJ_1@HC46	ARJ_1@C33	1	0.0002	2.9254	141.1673
ARG_189@HA	ARJ_1@HO7	ARJ_1@O10	1	0.0002	2.8220	168.2299
ARG_189@O	ARJ_1@HO6	ARJ_1@O9	1	0.0002	2.9947	137.5953
GLN_190@HB2	ARJ_1@HO6	ARJ_1@O9	1	0.0002	2.7595	141.5243
GLN_190@HG2	ARJ_1@HC45	ARJ_1@C32	1	0.0002	2.9558	138.1902
GLN_190@NE2	ARJ_1@HO6	ARJ_1@O9	1	0.0002	2.9174	171.8054

Table S7. Hydrogen bonding contacts between SARS-CoV-2 Mpro and CAN during the course of 50 ns MD simulation.

Acceptor	DonorH	Donor	Frames	Frac	AvgDist	AvgAng
LEU_168@O	CAR_1@H20	CAR_1@O4	1740	0.3480	2.7463	157.4539
MET_166@O	CAR_1@H19	CAR_1@O3	1420	0.2840	2.7375	158.8522
MET_150@O	CAR_1@H20	CAR_1@O4	1166	0.2332	2.7386	156.8742
TYR_55@O	CAR_1@H19	CAR_1@O3	1049	0.2098	2.7435	154.8205
GLU_167@OG1	CAR_1@H19	CAR_1@O3	461	0.0922	2.7967	156.7311
GLY_144@O	CAR_1@H20	CAR_1@O4	177	0.0354	2.8133	146.4497
CYS_146@HG1	CAR_1@H4	CAR_1@C5	67	0.0134	2.8788	145.5668
HIE_42@HE1	CAR_1@H5	CAR_1@C5	55	0.0110	2.9434	139.5184
HIE_166@HE22	CAR_1@H2	CAR_1@C4	55	0.0110	2.8396	145.3341
PRO_169@HA2	CAR_1@H18	CAR_1@C18	52	0.0104	2.9541	142.3784
THR_305@HG1	CAR_1@H19	CAR_1@O3	46	0.0092	2.9234	146.0978
ARG_299@HD2	CAR_1@H9	CAR_1@C9	37	0.0074	2.9540	142.8369
MET_7@HB2	CAR_1@H3	CAR_1@C4	34	0.0068	2.9436	140.6256
GLN_300@HE22	CAR_1@H15	CAR_1@C13	22	0.0044	2.8826	146.6258
THR_305@HA	CAR_1@H19	CAR_1@O3	16	0.0032	2.8504	142.0147
ASP_296@HB3	CAR_1@H15	CAR_1@C13	13	0.0026	2.9672	141.2950
THR_305@HG1	CAR_1@H24	CAR_1@C20	12	0.0024	2.8739	144.3733
ARG_299@HB3	CAR_1@H10	CAR_1@C9	11	0.0022	2.9476	140.5738
THR_305@HG21	CAR_1@H4	CAR_1@C5	11	0.0022	2.9517	139.0613
PHE_9@HE1	CAR_1@H6	CAR_1@C6	9	0.0018	2.9661	140.3801
GLN_300@O	CAR_1@H20	CAR_1@O4	9	0.0018	2.7691	153.2183

THR_305@HG22	CAR_1@H4	CAR_1@C5	8	0.0016	2.9435	137.4596
MET_7@HE1	CAR_1@H2	CAR_1@C4	7	0.0014	2.9515	138.8624
THR_305@HG23	CAR_1@H4	CAR_1@C5	7	0.0014	2.9334	137.4500
SER_302@OG	CAR_1@H20	CAR_1@O4	6	0.0012	2.8482	141.9877
SER_302@HG	CAR_1@H20	CAR_1@O4	6	0.0012	2.8939	144.2739
GLY_303@HA2	CAR_1@H23	CAR_1@C19	6	0.0012	2.9372	138.0174
PHE_9@HE1	CAR_1@H9	CAR_1@C9	5	0.0010	2.9414	140.6324
THR_305@HG21	CAR_1@H24	CAR_1@C20	5	0.0010	2.9552	138.8266
MET_7@HB3	CAR_1@H3	CAR_1@C4	4	0.0008	2.9826	142.9427
ALA_8@HA	CAR_1@H12	CAR_1@C12	4	0.0008	2.9482	143.1403
ASP_296@HA	CAR_1@H7	CAR_1@C6	4	0.0008	2.9510	146.5074
THR_305@HG21	CAR_1@H26	CAR_1@C20	4	0.0008	2.9477	141.3922
PHE_9@HD1	CAR_1@H11	CAR_1@C12	3	0.0006	2.9399	139.6092
GLN_300@HA	CAR_1@H21	CAR_1@C19	3	0.0006	2.9542	139.8735
GLN_300@HA	CAR_1@H23	CAR_1@C19	3	0.0006	2.9816	145.7792
GLN_300@HB3	CAR_1@H21	CAR_1@C19	3	0.0006	2.9546	137.7544
GLN_300@HE22	CAR_1@H1	CAR_1@C1	3	0.0006	2.8503	138.3940
SER_302@OG	CAR_1@H19	CAR_1@O3	3	0.0006	2.8134	141.3172
SER_302@HG	CAR_1@H19	CAR_1@O3	3	0.0006	2.9695	151.2527
MET_7@HB2	CAR_1@H2	CAR_1@C4	2	0.0004	2.9628	140.4048
MET_7@HB2	CAR_1@H16	CAR_1@C13	2	0.0004	2.9638	145.3214
MET_7@HG3	CAR_1@H8	CAR_1@C7	2	0.0004	2.9893	138.1837
ARG_299@HB2	CAR_1@H10	CAR_1@C9	2	0.0004	2.9649	139.2520
GLN_300@HB3	CAR_1@H23	CAR_1@C19	2	0.0004	2.9886	152.8275
GLN_300@HG2	CAR_1@H23	CAR_1@C19	2	0.0004	2.9764	138.0603
GLN_300@HG2	CAR_1@H1	CAR_1@C1	2	0.0004	2.9743	146.6264
GLY_303@HA2	CAR_1@H20	CAR_1@O4	2	0.0004	2.7769	145.4755
VAL_304@HA	CAR_1@H24	CAR_1@C20	2	0.0004	2.9104	137.6161
THR_305@HG22	CAR_1@H24	CAR_1@C20	2	0.0004	2.9688	137.3645
THR_305@HG1	CAR_1@H26	CAR_1@C20	2	0.0004	2.8944	138.1361
MET_7@HE1	CAR_1@H8	CAR_1@C7	1	0.0002	2.9954	140.2150
MET_7@HE2	CAR_1@H2	CAR_1@C4	1	0.0002	2.7989	139.4722
ALA_8@HA	CAR_1@H11	CAR_1@C12	1	0.0002	2.9834	141.6557
PHE_9@HD1	CAR_1@H5	CAR_1@C5	1	0.0002	2.9612	175.0720
GLN_128@HE21	CAR_1@H14	CAR_1@C13	1	0.0002	2.9814	154.4201
ASP_296@HB3	CAR_1@H7	CAR_1@C6	1	0.0002	2.9936	137.7998
ARG_299@HB3	CAR_1@H9	CAR_1@C9	1	0.0002	2.9274	135.7877
ARG_299@HE	CAR_1@H7	CAR_1@C6	1	0.0002	2.9138	135.4991
GLN_300@HA	CAR_1@H19	CAR_1@O3	1	0.0002	2.9414	157.6470
GLN_300@HA	CAR_1@H20	CAR_1@O4	1	0.0002	2.7519	143.9902
GLN_300@HB3	CAR_1@H22	CAR_1@C19	1	0.0002	2.9449	151.6648
GLN_300@HG3	CAR_1@H1	CAR_1@C1	1	0.0002	2.9637	148.8512
GLN_300@HE21	CAR_1@H15	CAR_1@C13	1	0.0002	2.9584	149.6626
GLN_300@HE22	CAR_1@H21	CAR_1@C19	1	0.0002	2.9714	142.9502
GLY_303@HA2	CAR_1@H21	CAR_1@C19	1	0.0002	2.8167	140.2891
VAL_304@H	CAR_1@H20	CAR_1@O4	1	0.0002	2.9891	140.6704
THR_305@HA	CAR_1@H20	CAR_1@O4	1	0.0002	2.8764	142.5832
THR_305@HA	CAR_1@H4	CAR_1@C5	1	0.0002	2.9841	175.2622
THR_305@HG22	CAR_1@H19	CAR_1@O3	1	0.0002	2.7647	136.8138
THR_305@HG23	CAR_1@H25	CAR_1@C20	1	0.0002	2.9848	155.2325
THR_305@HG23	CAR_1@H26	CAR_1@C20	1	0.0002	2.9867	136.5426
THR_305@HG1	CAR_1@H25	CAR_1@C20	1	0.0002	2.9560	164.9056

Table S8. Hydrogen bonding contacts between SARS-CoV-2 Mpro and ROS during the course of 50 ns MD simulation.

Acceptor	DonorH	Donor	Frames	Frac	AvgDist	AvgAng
GLU_167@O	ROS_1@HO5	ROS_1@O5	1869	0.3738	2.7711	156.4175
MET_166@HA	ROS_1@H52	ROS_1@C5	393	0.0786	2.9489	149.6561
GLN_190@HE21	ROS_1@H82	ROS_1@C8	77	0.0154	2.8696	144.8245
GLN_190@O	ROS_1@HO4	ROS_1@O4	43	0.0086	2.8511	150.9686
GLN_190@O	ROS_1@HO5	ROS_1@O5	28	0.0056	2.7946	157.9689
HIE_164@HE1	ROS_1@H123	ROS_1@C12	24	0.0048	2.9474	141.2026
SER_145@HG	ROS_1@H122	ROS_1@C12	22	0.0044	2.8813	139.3750
CYS_146@HB3	ROS_1@H83	ROS_1@C8	21	0.0042	2.9454	140.5712
CYS_146@HB2	ROS_1@H83	ROS_1@C8	16	0.0032	2.9434	140.1424
GLY_144@H	ROS_1@H133	ROS_1@C13	10	0.0020	2.8338	143.6150
PRO_169@HA	ROS_1@H193	ROS_1@C19	9	0.0018	2.9432	138.1336
ASN_143@HA	ROS_1@H133	ROS_1@C13	8	0.0016	2.9472	141.5629
SER_145@HG	ROS_1@H121	ROS_1@C12	8	0.0016	2.9374	139.1474
GLU_167@HG2	ROS_1@H192	ROS_1@C19	8	0.0016	2.9646	142.2156
CYS_146@HG	ROS_1@H82	ROS_1@C8	7	0.0014	2.9211	144.0154
ASN_143@HA	ROS_1@H132	ROS_1@C13	6	0.0012	2.9089	141.0412
ASN_143@HA	ROS_1@H131	ROS_1@C13	6	0.0012	2.9523	143.7351

ALA_192@HB1	ROS_1@H203	ROS_1@C20	6	0.0012	2.9472	140.2997
ALA_192@HB2	ROS_1@H203	ROS_1@C20	6	0.0012	2.9680	138.6066
SER_145@H	ROS_1@H122	ROS_1@C12	5	0.0010	2.9249	145.0947
CYS_146@H	ROS_1@H122	ROS_1@C12	5	0.0010	2.9272	140.0894
GLN_190@HE21	ROS_1@H52	ROS_1@C5	5	0.0010	2.8156	138.3265
CYS_146@HB2	ROS_1@H62	ROS_1@C6	4	0.0008	2.9628	135.2346
GLU_167@HG2	ROS_1@H193	ROS_1@C19	4	0.0008	2.9608	141.3301
PRO_169@HG3	ROS_1@H192	ROS_1@C19	4	0.0008	2.9734	136.7890
GLU_167@HG2	ROS_1@H191	ROS_1@C19	3	0.0006	2.9190	139.9954
CYS_146@HG	ROS_1@H83	ROS_1@C8	2	0.0004	2.8905	144.1501
CYS_146@HG	ROS_1@H62	ROS_1@C6	2	0.0004	2.9403	142.5780
HIE_164@HE1	ROS_1@H83	ROS_1@C8	2	0.0004	2.9832	158.4981
GLU_167@HB3	ROS_1@H193	ROS_1@C19	2	0.0004	2.9070	137.4495
PRO_169@HD3	ROS_1@H193	ROS_1@C19	2	0.0004	2.9636	137.0005
PRO_169@HG3	ROS_1@H191	ROS_1@C19	2	0.0004	2.9963	138.3463
PRO_169@HA	ROS_1@H192	ROS_1@C19	2	0.0004	2.9390	137.1062
ALA_192@HA	ROS_1@H192	ROS_1@C19	2	0.0004	2.9692	151.0106
ALA_192@HB1	ROS_1@H202	ROS_1@C20	2	0.0004	2.9304	144.9613
ALA_192@HB2	ROS_1@H202	ROS_1@C20	2	0.0004	2.8988	142.6836
ALA_192@HB3	ROS_1@H203	ROS_1@C20	2	0.0004	2.9794	142.7595
LEU_142@HA	ROS_1@H4	ROS_1@C4	1	0.0002	2.9768	164.5189
ASN_143@HA	ROS_1@H122	ROS_1@C12	1	0.0002	2.9495	142.9529
CYS_146@HB2	ROS_1@H122	ROS_1@C12	1	0.0002	2.9903	135.0644
GLU_167@HB3	ROS_1@H191	ROS_1@C19	1	0.0002	2.9344	138.5099
PRO_169@HG3	ROS_1@H193	ROS_1@C19	1	0.0002	2.8810	139.5311
PRO_169@HB3	ROS_1@H191	ROS_1@C19	1	0.0002	2.9974	143.5203
ALA_192@HA	ROS_1@H191	ROS_1@C19	1	0.0002	2.9882	137.0641
ALA_192@HA	ROS_1@H193	ROS_1@C19	1	0.0002	2.9407	151.3128
ALA_192@HA	ROS_1@H201	ROS_1@C20	1	0.0002	2.9733	147.9794
ALA_192@HA	ROS_1@HO5	ROS_1@O5	1	0.0002	2.9995	138.3159
ALA_192@HA	ROS_1@H203	ROS_1@C20	1	0.0002	2.9593	140.6071
ALA_192@HB1	ROS_1@H201	ROS_1@C20	1	0.0002	2.9944	141.7106
ALA_192@HB1	ROS_1@HO5	ROS_1@O5	1	0.0002	2.7851	141.1014
ALA_192@HB2	ROS_1@H201	ROS_1@C20	1	0.0002	2.9540	145.2316
ALA_192@HB3	ROS_1@H202	ROS_1@C20	1	0.0002	2.9755	136.4202

Table S9. The various components of the Binding Free Energy (kcal mol^{-1}) evaluated by the Molecular Mechanics-Generalized Borne Surface Area (MM-GBSA) method between the SARS-CoV-2 main protease(Mpro) – alpha ketoamide(AKA) complex.

	Mpro-AKA		Mpro		AKA		▲	
	Average	std. dev. (±)	average	std. dev. (±)	average	std. dev. (±)	average	std. dev. (±)
VDW	-2403.67	21.29	-2363.27	21.30	-1.83	1.58	-38.57	1.84
ELE	-21647.22	41.98	-21576.06	42.28	-58.59	1.50	-12.56	3.88
GB	-2610.86	18.74	-2601.34	18.87	-19.29	0.98	9.77	3.70
GBSUR	103.86	1.02	105.04	1.03	3.36	0.01	-4.54	0.01
GAS	-24050.90	37.31	-23939.33	37.89	-60.43	2.34	-51.13	4.09
GBSOL	-2506.99	18.87	-2516.29	19.01	-15.92	0.98	25.22	3.65
GBTOT	-26557.89	34.87	-26445.63	34.92	-76.35	2.48	-35.90	2.02
TSTRA	17.01	0.00	16.99	0.00	13.42	0.00	-13.40	0.00
TSTRO	17.72	0.01	17.70	0.01	11.43	0.01	-11.41	0.01
TSVIB	3314.02	3.69	3258.52	4.41	53.45	0.25	2.05	2.56
TSTOT	3348.75	3.70	3293.22	4.42	78.30	0.26	-22.76	2.57
ΔG_{bind}							**-13.14**	

Electrostatic energy (**ELE**); van der Waals contribution (**VDW**); total gas-phase energy (**GAS**); nonpolar contribution to the solvation free energy (**GBSUR**); the electrostatic contribution to the solvation free energy (**GB**); sum of nonpolar and polar contributions to solvation (**GBSOL**); final estimated binding free energy (**GBTOT**); translational energy (**TSTRA**); rotational energy (**TSROT**); vibrational energy (**TSVIB**), total entropic contribution (**TSTOT**); binding free energy (**ΔG_{bind}**).

Table S10. The various components of the Binding Free Energy (kcal mol^{-1}) evaluated by Molecular Mechanics-Poisson-Boltzmann Surface Area (MM-PBSA) method between SARS-CoV-2 main protease(Mpro) – alpha ketoamide(AKA) complex.

	Mpro-AKA		Mpro		AKA		▲	
	Average	Std. Dev. (±)	Average	Std. Dev. (±)	Average	Std. Dev. (±)	Average	Std. Dev. (±)
VDW	-2403.67	21.29	-2363.27	21.30	-1.83	1.58	-38.57	1.84
ELE	-21647.22	41.98	-21576.06	42.28	-58.59	1.50	-12.56	3.88
PB	-2650.11	17.74	-2664.57	18.14	-21.09	0.84	35.55	3.09
NPOLAR	2328.40	4.98	2376.58	4.90	37.43	0.19	-85.43	0.63
DISPER	-1307.40	5.76	-1314.42	5.68	-35.99	0.17	43.01	0.65
GAS	-24050.90	37.31	-23939.33	37.89	-60.43	2.34	-51.13	4.09
PBSOL	-1629.11	18.19	-1662.51	18.76	-19.65	0.84	53.06	3.29
PBTOL	-25680.01	37.08	-25570.76	37.48	-80.08	2.24	-28.07	3.41
TSTRA	17.01	0.00	16.99	0.00	13.42	0.00	-13.40	0.00
TSTRO	17.72	0.01	17.70	0.01	11.43	0.01	-11.41	0.01
TSVIB	3314.02	3.69	3258.52	4.41	53.45	0.25	2.05	2.56
TSTOL	3348.75	3.70	3293.22	4.42	78.30	0.26	-22.76	2.57
ΔG_{bind}								**-5.31**

Electrostatic energy (**ELE**); van der Waals contribution (**VDW**); total gas phase energy (**GAS**); nonpolar contribution to the solvation free energy (**GBSUR**); the electrostatic contribution to the solvation free energy (**GB**); sum of nonpolar and polar contributions to solvation (**GBSOL**); final estimated binding free energy (**GBTOT**); translational energy (**TSTRA**); rotational energy (**TSROT**); vibrational energy (**TSVIB**), total entropic contribution (**TSTOT**); binding free energy (**ΔG_{bind}**).

Table S11. The various components of the Binding Free Energy (kcal mol^{-1}) evaluated by the Molecular Mechanics-Generalized Borne Surface Area (MM-GBSA) method between SARS-CoV-2 main protease(Mpro)–arjunglucoside-I(ARJ) complex.

	Mpro-ARJ		Mpro		ARJ		▲	
	average	std. dev. (±)	average	std. dev. (±)	average	std. dev. (±)	average	std. dev. (±)
VDW	-2354.72	20.03	-2318.97	19.68	-1.78	1.51	-33.96	1.84
ELE	-21639.86	36.00	-21531.04	36.41	-94.56	2.30	-14.25	5.63
GB	-2619.47	25.94	-2592.13	26.27	-23.86	2.33	-3.48	3.89
GBSUR	107.75	0.92	108.00	0.93	3.46	0.01	-3.71	0.13
GAS	-23994.59	39.83	-23850.02	39.84	-96.35	3.00	-48.21	4.76
GBSOL	-2511.71	25.50	-2514.12	25.79	-20.40	2.33	22.81	3.91
GBTOT	-26506.30	36.48	-26349.14	36.81	-116.75	2.59	-40.39	1.65
TSTRA	17.01	0.00	16.99	0.00	13.51	0.00	-13.50	0.00
TSTRO	17.73	0.00	17.71	0.00	11.75	0.00	-`11.73	0.00
TSVIB	3328.01	5.23	3272.04	5.44	51.38	0.04	4.58	2.75
TSTOT	3362.75	5.23	3306.75	5.44	76.65	0.04	-20.65	2.75
ΔG_{bind}								**-19.74**

Table S12. The various components of the Binding Free Energy (kcal mol^{-1}) evaluated by the Molecular Mechanics-Poisson-Boltzmann Surface Area (MM-PBSA) method between SARS-CoV-2 main protease(Mpro)–arjunglucoside-I (ARJ) complex.

	Mpro-ARJ		Mpro		ARJ		Delta	
	Average	Std. Dev. (±)	Average	Std. Dev. (±)	Average	Std. Dev. (±)	Average	Std. Dev. (±)
VDW	-2354.72	20.03	-2318.97	19.68	-1.78	1.51	-33.96	1.84
ELE	-21639.86	36.00	-21531.04	36.41	-94.56	2.30	-14.25	5.63
PB	-2649.89	19.86	-2658.20	20.54	-26.25	2.54	34.56	3.95
NPOLAR	2356.32	6.28	2410.29	6.22	37.98	0.18	-91.95	0.62
DISPER	-1345.89	5.34	-1349.73	5.54	-36.98	0.19	40.82	0.60
GAS	-23994.59	39.83	-23850.02	39.84	-96.35	3.00	-48.21	4.76
PBSOL	-1639.46	19.85	-1667.64	20.77	-25.25	2.53	53.43	4.11
PBTOL	-25634.05	36.40	-25481.67	35.97	-121.60	2.79	-29.78	3.09
TSTRA	17.01	0.00	16.99	0.00	13.51	0.00	-13.50	0.00
TSTRO	17.73	0.00	17.71	0.00	11.75	0.00	-`11.73	0.00
TSVIB	3328.01	5.23	3272.04	5.44	51.38	0.04	4.58	2.75
TSTOL	3362.75	5.23	3306.75	5.44	76.65	0.04	-20.65	2.75
ΔG_{bind}								**-9.13**

Table S13. The various components of the Binding Free Energy (kcal mol^{-1}) evaluated by the Molecular Mechanics-Generalized Borne Surface Area (MM-GBSA) method between the SARS-CoV-2 main protease(Mpro) – Carsonol(CAN) complex.

	Mpro-CAN		Mpro		CAN		▲	
	average	std. dev. (±)	average	std. dev. (±)	average	std. dev. (±)	average	std. dev. (±)
VDW	-2371.15	19.04	-2325.41	18.49	-1.60	1.59	-44.13	1.43
ELE	-21486.26	47.68	-21408.65	47.56	-59.01	1.65	-18.60	2.13
GB	-2790.09	28.48	-2803.01	27.87	-19.54	1.22	32.46	1.67
GBSUR	-110.37	0.78	-111.65	0.78	3.37	0.02	-4.65	0.16
GAS	-23857.42	46.58	-23734.06	46.09	-60.61	2.30	-62.47	2.42
GBSOL	-2679.72	28.46	-2691.36	27.89	-16.17	1.23	27.81	1.68
GBTOT	-26537.14	38.86	-26425.43	38.16	-76.78	2.38	-34.93	1.78
TSTRA	17.01	0.00	16.99	0.00	12.89	0.00	-12.88	0.00
TSTRO	17.71	0.01	17.71	0.00	10.32	0.00	-10.32	0.01
TSVIB	3294.63	7.24	3268.39	5.11	21.15	0.01	5.08	4.31
TSTOT	3329.35	7.24	3303.11	5.11	44.37	0.01	-18.12	4.32
ΔG_{bind}								**-16.81**

Table S14. The various components of the Binding Free Energy (kcal mol^{-1}) evaluated by Molecular Mechanics-Poisson-Boltzmann Surface Area (MM-PBSA) method between SARS-CoV-2 main protease(Mpro) – carsonol(CAN complex).

	Mpro-CAN		Mpro		CAN		▲	
	average	std. dev. (±)	average	std. dev. (±)	average	std. dev. (±)	average	std. dev. (±)
VDW	-2371.15	19.04	-2325.41	18.49	-1.60	1.59	-44.13	1.43
ELE	-21486.26	47.68	-21408.65	47.56	-59.01	1.65	-18.60	2.13
PB	-2838.37	27.09	-2849.99	27.07	-21.30	0.89	32.92	2.02
NPOLAR	2362.69	3.81	2393.40	4.03	37.32	0.15	-68.03	0.73
DISPER	-1351.53	3.41	-1365.30	3.54	-35.96	0.15	49.74	0.45
GAS	-23857.42	46.58	-23734.06	46.09	-60.61	2.30	-62.74	2.42
PBSOL	-1827.20	27.43	-1861.89	27.53	-19.95	0.92	54.63	2.37
PBTOL	-25684.63	36.70	-25575.96	36.43	-80.56	2.30	-28.10	2.78
TSTRA	17.01	0.00	16.99	0.00	12.89	0.00	-12.88	0.00
TSTRO	17.71	0.01	17.71	0.00	10.32	0.00	-10.32	0.01
TSVIB	3294.63	7.24	3268.39	5.11	21.15	0.01	5.08	4.31
TSTOL	3329.35	7.24	3303.11	5.11	44.37	0.01	-18.12	4.32
ΔG_{bind}								**-9.98**

Table S15. The various components of the Binding Free Energy (kcal mol^{-1}) evaluated by the Molecular Mechanics-Generalized Borne Surface Area (MM-GBSA) method between the SARS-CoV-2 main protease(Mpro)-Rosmanol(ROS) complex.

	Mpro-ROS		Mpro		ROS		▲	
	average	std. dev. (±)	average	std. dev. (±)	average	std. dev. (±)	average	std. dev. (±)
VDW	-2349.32	20.11	-2316.12	19.82	-1.42	1.80	-31.77	1.89
ELE	-21530.17	38.52	-21413.80	39.24	-95.14	2.13	-21.22	2.97
GB	-2709.64	21.53	-2698.31	21.89	-23.17	1.90	11.84	2.83
GBSUR	111.81	0.98	111.40	0.97	3.46	0.01	-3.04	0.01
GAS	-23879.49	40.27	-23729.93	41.31	-96.57	3.04	-52.99	3.44
GBSOL	-2597.82	21.21	-2606.91	21.57	-19.70	1.90	28.79	2.80
GBTOT	-26477.32	32.22	-26326.84	32.53	-116.27	2.70	-34.19	2.33
TSTRA	17.01	0.00	16.99	0.00	12.93	0.00	-12.92	0.00
TSTRO	17.72	0.00	17.71	0.00	10.39	0.00	-10.38	0.00
TSVIB	3282.50	5.29	3257.09	4.31	22.23	0.08	3.16	6.74
TSTOT	3317.22	5.29	3291.80	4.31	45.56	0.08	-20.14	6.74
ΔG_{bind}								**-14.05**

Table S16. The various components of the Binding Free Energy (kcal mol^{-1}) evaluated by the Molecular Mechanics-Poisson-Boltzmann Surface Area (MM-PBSA) method between the SARS-CoV-2 main protease(Mpro)-Rosmanol(ROS) complex.

	Mpro-ROS		Mpro		ROS		▲	
	average	std. dev. (±)	average	std. dev. (±)	average	std. dev. (±)	average	std. dev. (±)
VDW	-2349.32	20.11	-2316.12	19.82	-1.42	1.80	-31.78	1.89
ELE	-21530.17	38.52	-21413.80	39.24	-95.14	2.13	-21.23	2.97
PB	-2736.89	26.34	-2748.61	26.33	-25.20	1.88	36.92	3.12
NPOLAR	2368.27	7.08	2405.68	7.20	37.97	0.15	-75.38	0.63
DISPER	-1364.39	6.31	-1365.04	6.48	-36.80	0.19	37.45	0.80
GAS	-23879.49	40.27	-23729.93	41.31	-96.57	3.04	-52.99	3.44
PBSOL	-1733.01	26.82	-1763.97	26.61	-24.03	1.82	**54.98**	3.21
PBTOL	-25612.51	40.47	-25434.90	40.59	-120.60	2.75	-26.01	2.56
TSTRA	17.01	0.00	16.99	0.00	12.93	0.00	-12.92	0.00
TSTRO	17.72	0.00	17.71	0.00	10.39	0.00	-10.38	0.00
TSVIB	3282.50	5.29	3257.09	4.31	22.23	0.08	3.16	6.74
TSTOL	3317.22	5.29	3291.80	4.31	45.56	0.08	-20.14	6.74
ΔG_{bind}								**-5.87**